Monatshefte für Chemie 136, 925–963 (2005)
DOI 10.1007/s00706-005-0310-2

Monatshefte für Chemie
Chemical Monthly
Printed in Austria

Invited Review

Chemical Bonding in Molecules and Complexes Containing d-Elements Based on DFT

Mihail Atanasov[1,2,*], **Claude A. Daul**[2,*], and **E. Penka Fowe**[2]

[1] Institute of General and Inorganic Chemistry, Bulgarian Academy of Sciences, 1113 Sofia, Bulgaria
[2] Department of Chemistry, University of Fribourg, CH-1700 Fribourg, Switzerland

Received December 6, 2004; accepted January 17, 2005
Published online May 23, 2005

Summary. Metal–ligand bonding in transition metal halide molecules and complexes with different central ions, oxidations states, and coordination numbers: $Cr^{III}X_6^{3-}$, $Cr^{IV}X_4$, $Cr^{II}X_2$ (X = F,Cl,Br,I), $M^{III}Cl_6^{3-}$ (M = Mo,W), $M^{III}(H_2O)_6^{3+}$ (M = Cr,Co) and $Re_2Cl_8^{2-}$ has been studied in terms of the Extended Transition State (ETS) energy patitioning scheme within the DFT and electron density analysis (the Laplacian of the electron density and the electronic localization function). Bonding is found to be dominated by ionicity in all cases, especially so for complexes with higher coordination numbers. Covalent contributions to the metal–ligand bond are found to be mainly due to the nd-electrons and to lesser extent due to the metal (n + 1)s and (n + 1)p-orbitals, contributions from (n + 1)s increasing when going to lower coordination numbers. Metal–ligand bonding analysis have been used in order to check some concepts emerging from ligand field theory when applied to the spectroscopy and magnetism of transition metal complexes. It is pointed out that for complexes of high symmetry (MX_6, O_h, MX_4, T_d, and MX_2, $D_{\infty h}$) electron density analyses gain interpretative power when partitioned into contributions from occupied orbitals of different symmetry.

Keywords. DFT; Energy decomposition analysis (EDA); Laplacian of the electron density; Electronic localization function (ELF); Angular overlap model (AOM).

I. Introduction

Chemical bonding in Transition Metal (TM) complexes has been intensively studied by experimental and theoretical methods. Difference density analysis as derived by highly resolved X-ray crystallography [1] and later modern quantum chemistry

* Corresponding author. E-mails: claude.daul@unifr.ch; mihail.atanasov@unifr.ch

calculations (MO-theory – *ab-initio*, *Morokuma* [2], DFT [3] – or valence-bond theory, *Pauling* [4–6]) provide important insight into the nature of the metal–ligand bond. An extensive review on quantum chemical methods for analyzing the chemical bond and their applications to a wide range of closed shell TM complexes with organic ligands (carbene, carbyne, alkene, and alkyne π-complexes) as well as complexes with CO, BF, BO^-, BNH_2, and H ligands has been published by *Frenking* and *Fröhlich* [7] and we refer the reader to their work.

In this study we would like to concentrate on the chemical bonding in open-shell molecules and complexes of TM with halide (X = F,Cl,Br,I) and H_2O ligands which are less well studied theoretically. In our analysis we include complexes of TM-ions with different oxidation states II(Cr–d^4), III(Cr, Mo, W–d^3, Co–d^6, and Re–d^4), and IV(Cr–d^2) as well as different Coordination Numbers (CN=6,4, and 2). The species studied are depicted in Fig. 1 along with their geometries.

For complexes with open d-shells, electronic structure has been studied experimentally using UV-VIS electronic absorption, emission, and EPR spectroscopies. The most broadly used bonding model for these compounds has been ligand field theory (LFT). This is an orbital interaction model which focuses on the d-orbitals of the TM and the valence p- and s-orbitals on the ligands. A reference point of discussion in LFT is the interaction between one TM cation and the surrounding ligands. For ligand-to-metal donor–acceptor bonds, LFT leads to destabilization of the metal $|nd\rangle$ and to a stabilization of the ligand $|s\rangle$ and $|p\rangle$ atomic orbitals to give rise to antibonding and bonding molecular orbitals of the resulting complex, respectively. A simplified version of the LFT theory has been the Angular Overlap Model (AOM), which considers the splitting of the TM d-orbitals as resulting from overlap with the ligands. The energies of this splitting could be deduced from the interpretations of spectra and lead to a classification of ligands according to their σ and π-donor properties. Thus, from a series of complexes $Cr(NH_3)_5X$,

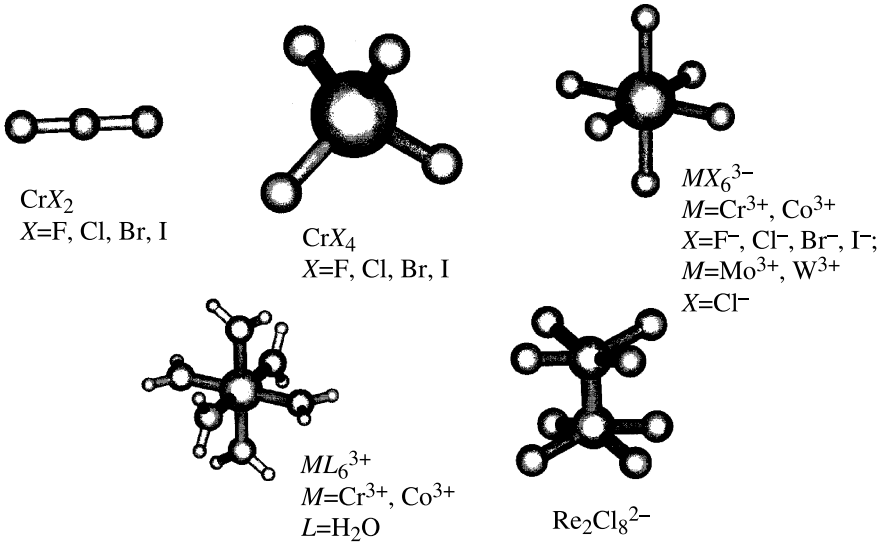

Fig. 1. Transition metal molecules and complexes and their structures studied in this work

$X = $ F,Cl,Br,I, and H_2O a classification of these ligands was possible based on values of the corresponding energy parameters – e_σ and e_π [8, 9].

In LFT, information about the metal ligand bond is obtained from a consideration of the electronic states originating from a more or less well defined d^n electronic configuration to allow application of perturbation theory and overlap considerations when calculating the multiplet structure. Contributions of $|4s\rangle$ and $|4p\rangle$ orbitals to the bonding are generally ignored. Semi-empirical LF parameters derived from the spectra of these complexes involve both ground and excited state contributions resulting from electron replacements within the antibonding $|nd\rangle$ orbitals. However, bonding in molecules and complexes is mostly governed by bonding electronic interactions. Being beyond the reach of UV-VIS spectroscopies, those interactions can only be studied using quantum-chemical, first principle methods. The bonding analysis of the present study makes use of the extended transition state method (ETS) by *Bickelhaupt* and *Baerends* [3b] as implemented in the Amsterdam DFT (ADF) program [10]. It allows to decompose the bonding energy between the constituting fragments into chemically meaningful components. A drawback of this method is the need of selecting starting fragments (pro-molecule) with a proper electronic configuration, and – in case of polyatomic ligands – with the corresponding geometry. Chemical intuition and experience has to be invoked when choosing fragments for such analysis. In view of this, in addition to the ETS method, we have chosen another method in our analysis. It is based on the pioneering work of *R. Bader* [11] which allows to define atoms within molecules in an unique and quantum-mechanically well justified way. The only piece of information needed for such analysis is the Laplacian of the electron density which is also available from DFT.

Finally, we use another closely related quantity – the electron localization function (ELF) introduced by *Becke* and *Edgecombe* [12] and refined and applied by *Savin*, *Silvi*, and *Kohout* [13–15] to obtain a pictorial representation of the underlying metal–ligand bonding interactions. The topological analysis of the electron localization function [16a–16c] is intended to provide a direct space mathematical model to the *Lewis* theory and the valence state electron pair repulsion (VSEPR) model of *Gillespie* and *Nyholm*. It further allows to propose non-ambiguous definitions of covalent and dative bonds thus making it possible to apply the model to analysis of bonding in TM complexes [16d].

This work is structured as follows. In Sections II we briefly present the basic ideas behind the ETS method (Section II.1), the topological analysis of the chemical bond (*Bader* analysis, Sections II.2.1), and the electronic localization function (Section II.2.2). In Section II.3, the AOM for the cases studied in this work is presented, followed by a closing computational Section II.4. In Sections III we present our results considering TM complexes in the order of decreasing coordination number (CN=6, Section III.1; CN=4, Section III.2; CN=2, Section III.3). Finally, the bonding in $Re_2Cl_8^{2-}$ will be discussed in detail with special emphasize on the influence of the Re–Cl interactions on the Re–Re bonds (Section III.4). In a concluding Section IV we will discuss the effect of the CN, of the oxidation state, and of the nature of the TM within a period or within a group of the periodic table. The importance of $|(n+1)s\rangle$ and $|(n+1)p\rangle$ valence orbitals of the TM for the metal to ligand bond is re-addressed and discussed. Here, we also compare the

overall attractive part of the metal–ligand bonding, with that part due to the repulsive antibonding |nd⟩-electrons only, thus aiming to connect chemical bonding and ligand field spectroscopy. At this place we quote the seminal book of *C. K. Jørgensen*, ''Absorption spectra and chemical bonding'' [17] in which many original ideas have been proposed, but an exhaustive theoretical analysis was lacking at that time. It is the ambitious task of the present study to fill this gap using modern DFT and recent bond theoretical developments.

II. Theory

II.1. The Extended Transition State Method (ETS)

The ETS method [3b] which is equivalent to the energy decomposition analysis of *Morokuma et al.* [2], starts from an intermediate state between that of the non-interacting fragments and the product molecule. In this state (pro-molecule) the electron densities of molecular subunits are taken as frozen at their actual positions within the molecule and the electrostatic interaction energy $\Delta E_{\mathrm{Elstat}}$ between electrons and nuclei is calculated classically. It is usually a negative quantity reflecting attractive forces. The resulting fragment wavefunctions are non-orthonormal. In a second step an ortogonalisation and an antisymmetrisation is carried out in order to obtain a wavefunction which obeys the *Pauli*'s principle. The energy ΔE_{Pauli} calculated using this function, is called the *Pauli* (exchange) repulsion. The resulting hypothetical state is called the transition state (TS). In a third step the TS is fully relaxed during an SCF procedure and yields the electron density and the energy of the molecule in its final ground state. The gain of energy due to orbital relaxation, ΔE_{orb} along with the $\Delta E_{\mathrm{Elstat}}$ term are the driving forces which lead from the preselected frozen fragments to the final molecule. The orbital relaxation term is due to electron transfer from doubly and singly occupied orbitals of a given fragment to empty or half filled orbitals of neighbouring fragments and reflects electron delocalization (covalency). It bears valuable chemical information, because, in higher symmetric molecules, ΔE_{orb} can be further decomposed into orbital contribution of different symmetry and does allow bond-analysis in terms of σ and π-contributions. In cases like this, transition-metal fragments can be considered as being of cylindrical symmetry as in the AOM, which has been applied so successfully to analyze analogous effects for antibonding d-orbitals. The ΔE_{orb} energy contains also terms due to excitation of electrons from occupied to empty orbitals *within the same fragment*. This is orbital polarization energy and reflects mixing of fragment orbitals due to symmetry lowering when going from the separate fragments to their ultimate positions in the molecule. This is similar to the d-orbital splitting considered in crystal field theory. Unfortunately, charge-polarization and charge-transfer are unseparable in this description. Finally, it should be pointed out that both metal and ligands will need some adjustment of their valence (oxidation) states which will bring them in a state where interaction with other fragments is particularly favored. The corresponding energy, the preparation energy ΔE_{Prep} is of electronic and/or geometric origin and has to be calculated before setting up the promolecule. Such a possibility is offered by the Amsterdam Density Functional packages where molecules are always calculated starting from reference fragments.

We thus end-up with an expression for the energy ΔE of the reaction, say $A + B \rightarrow AB$, as shown by Eq. (1).

$$\begin{aligned} \Delta E &= E(AB) - E(A) - E(B) = \Delta E_{\text{prep}} + \Delta E_{\text{int}} \\ &= \Delta E_{\text{prep}} + \Delta E_{\text{Elstat}} + \Delta E_{Pauli} + \Delta E_{\text{orb}} \end{aligned} \quad (1)$$

In Table 1 we include some prototype examples for ETS analysis for H_2, NaCl, and F_2 which are particularly useful in view of the following discussion (*vide infra*). In all cases, taking atoms in their ground states as reference fragments, ΔE_{orb} is the dominating energy term in ΔE_{int} ($\Delta E_{\text{prep}} = 0$ in these cases). It consists of negative bonding terms, and sometimes strongly positive antibonding ones: such as $\Delta E_{\text{orb}}(\sigma_g)$ and $\Delta E_{\text{orb}}(\sigma_u)$ for F_2, respectively. However there are also negative terms due to orbital polarization: the energies ΔE_{orb} (π_g) and ΔE_{orb} (π_u) for the π_g orbitals of F_2, which being, doubly occupied, should not contribute to the bonding.

It should be pointed out that the outcome of an ETS analysis depends stongly on the chosen fragments. Thus, for H_2, taking H fragments with a single electron on each, there must be no ΔE_{Pauli} terms. As seen from inspection of Table 1, this is only fulfilled when using spin-polarised fragments allowing α and β spins to localize on different atoms resulting from a symmetry breaking from $D_{\infty h}$ to $C_{\infty v}$. This is less pronounced for atoms with more than 1 electron. Thus, for F_2, very similar results are obtained comparing calculations with spin-restricted or spin-unrestricted fragments. However, the situation changes when one has to make a choice between neutral and ionic fragments. Thus, for NaCl a rather different result is obtained when comparing calculations for atomic [Na, Cl] and ionic [Na^+, Cl^-] fragments

Table 1. Energy decomposition analysis for H_2, NaCl, and F_2 using the ETS method[a]

Molecule	H_2		NaCl		F_2
gr.state electr. configuration	σ_g^2	σ^2	$\sigma^4\pi^4$		$\sigma_g^4\sigma_u^2\pi_g^4\pi_u^4$
reference fragments	$H(1s^1)$		$Na(2s^1)$	Na^+	$F(2s^22p^5)$
	$H(1s^1)$		$Cl(2s^22p^5)$	Cl^-	$F(2s^22p^5)$
	restr.	unrestr.			
ΔE_{Pauli}[b]	10.03	−0.58	2.55	0.97	12.20
ΔE_{Elstat}[b]	0.26	0.27	−1.33	−6.16	−3.67
ΔE_{orb}[b]	−17.08	−4.31	−5.70	−0.63	−12.08
ΔE_{int}[b]	−6.79	−4.62	−4.47	−5.82	−3.55
$\Delta E_{\text{int}}'$[c]	−4.55	–	−4.04	−5.82	−2.73
ΔE_{prep}[d]	–		–	1.78	
orbital increments of ΔE_{orb}[b]	σ_g −12.97		σ −0.80	−0.37	σ_g −5.81
		σ −4.31	π −4.91	−0.26	σ_u 8.58
	σ_u −4.11				π_g −6.30
					π_u −8.54

[a] Geometry optimizations using a *PW*91 functional; bond distances (Å): H–H 0.749, NaCl 2.420, F–F 1.433; [b] with respect to spin-restricted atomic fragments; [c] with respect to atomic fragments in their spin-unrestricted ground states: ^{2}S(H), −1.12 eV, ^{2}S(Na) −0.21 eV, ^{2}P(Cl) −0.22 eV, ^{2}P(F) −0.41 eV; [d] $\Delta E_{\text{prep}}(\text{NaCl}) = E(Na^+) - E(^2\text{S, Na}) + E(Cl^-) - E(^2\text{P, Cl}) = 5.19 - (-0.21) + (-3.84) - (-0.22) = 1.78$ eV

(Table 1). In the latter case, bonding is dominated strongly by ionic forces (the ΔE_{Elstat} term), while the sum of $\Delta E_{\text{orb}} + \Delta E_{Pauli}$ is nearly vanishing. It is ionic bonding which is the driving force for the formation of ionic solids, such as NaCl, and it has been shown that lattice energies of ionic crystals are dominated by 99% by electrostatic (*Madelung*) energy. We notice, that going from atomic to ionic fragments, requires a significant preparation energy, which for NaCl consists of the energy for the $^2\text{S(Na)} \rightarrow \text{Na}^+$ transition minus the energy gained by the $^2\text{P(Cl)} \rightarrow \text{Cl}^-$ process. Considerations like this trace the essential steps of the well known *Born-Haber* cycle used for calculation of the lattice energy in ionic crystals.

II.2. Bonding Schemes Based on the Electron Density and its Analysis

II.2.1. The Laplacian of the Electron Density (Bader Analysis) and its Resolution into Orbital Symmetry Components

Valuable information about the chemical bond can be obtained from the electron density, which is in principle an observable quantity, and its analysis which is the subject of the "Atoms in Molecule" (AIM) method by *R. Bader* [11]. Let us assume that we know the electron density in every points of space, $\rho(x, y, z)$. Focussing on an arbitrary but fixed point in space (x_o, y_o, z_o) we can expand ρ in a *Taylor* series (Eq. (2)).

$$\begin{aligned}
&\rho(x_o + \delta x, y_o + \delta y, z_o + \delta z) \\
&\quad = \rho(x_o, y_o, z_o) + \left(\frac{\partial \rho}{\partial x}\right)_{xo} \delta x + \left(\frac{\partial \rho}{\partial y}\right)_{yo} \delta y + \left(\frac{\partial \rho}{\partial z}\right)_{zo} \delta z \\
&\qquad + \frac{1}{2}\left(\frac{\partial^2 \rho}{\partial x^2}\right)_{xo} \delta x^2 + \frac{1}{2}\left(\frac{\partial^2 \rho}{\partial y^2}\right)_{yo} \delta y^2 + \frac{1}{2}\left(\frac{\partial^2 \rho}{\partial z^2}\right)_{zo} \delta z^2 \\
&\qquad + \left(\frac{\partial^2 \rho}{\partial x \partial y}\right)_{xo,\, yo} \delta x \delta y + \left(\frac{\partial^2 \rho}{\partial x \partial z}\right)_{xo,\, zo} \delta x \delta z + \left(\frac{\partial^2 \rho}{\partial y \partial z}\right)_{yo,\, zo} \delta y \delta z \qquad (2)
\end{aligned}$$

Fig. 2. (a) Contour plots of the Laplacian constructed using the total electron density for the H_2, NaCl, and F_2 molecules; values for the Laplacian (second derivative of the density, taken with a minus sign) at the bond critical points (L_{bcp}) are included to show the overall charge concentration (in the case of H_2) and charge depletion (in the case of NaCl and F_2); contour plots are constructed using program tools cited under Ref. [11b] and contour lines depicted using (default) values of the Laplacian of the electron density (-0.02, -0.04, -0.08, -0.20, -0.40, -0.80, -2.00, -4.00, -8.00, -10.00, 0.0, 0.02, 0.04, 0.08, 0.20, 0.40, 0.80, 2.00, 4.00, 8.00, 10.00); negative (charge depletion) and positive (charge concentration) values are plotted with solid and dashed lines, respectively; (b) Contour plots for the electron density (ρ) and Laplacian (L, negative of second derivative) of the electron density for F_2, decomposed into σ ($\sigma_g + \sigma_u$) and π ($\pi_g + \pi_u$) symmetry components; L values for the bond critical points (L_{bcp}), for the σ-plot, and the ring and cage critical points (L_{rcp}, L_{ccp}, respectively, for the π-plot) are included; contour plots are constructed using program tools cited under Ref. [11b] and contour lines depicted using (default) values of the Laplacian of the electron density (-0.02, -0.04, -0.08, -0.20, -0.40, -0.80, -2.00, -4.00, -8.00, -10.00, 0.0, 0.02, 0.04, 0.08, 0.20, 0.40, 0.80, 2.00, 4.00, 8.00, 10.00); negative and positive values are plotted with solid and dashed lines, respectively; plots of the density are given using default values (0.001, 0.002, 0.004, 0.008, 0.02, 0.04, 0.08, 0.20, 0.40, 0.80, 2.00, 4.00, 8.00, 20.00, 40.00, 80.0 with values increasing from the outer to the inner region of the molecule)

The first and second derivatives in Eq. (2) define a vector $\overrightarrow{\nabla\rho}$ and a (symmetric) matrix of second derivative (Hessian) H (Eq. (3)).

$$(\overrightarrow{\nabla\boldsymbol{\rho}})_{\mathbf{r0}} = \begin{pmatrix} \left(\frac{\partial\rho}{\partial x}\right)_{xo} \\ \left(\frac{\partial\rho}{\partial y}\right)_{yo} \\ \left(\frac{\partial\rho}{\partial z}\right)_{zo} \end{pmatrix}; \quad (\mathrm{H})_{\mathbf{r0}} = \begin{bmatrix} \left(\frac{\partial^2\rho}{\partial x^2}\right)_{xo} & \left(\frac{\partial^2\rho}{\partial x\partial y}\right)_{xo,\,yo} & \left(\frac{\partial^2\rho}{\partial x\partial z}\right)_{xo,\,zo} \\ \left(\frac{\partial^2\rho}{\partial y\partial x}\right)_{yo,\,xo} & \left(\frac{\partial^2\rho}{\partial y^2}\right)_{yo} & \left(\frac{\partial^2\rho}{\partial y\partial z}\right)_{yo,\,zo} \\ \left(\frac{\partial^2\rho}{\partial z\partial x}\right)_{zo,\,xo} & \left(\frac{\partial^2\rho}{\partial z\partial y}\right)_{zo,\,yo} & \left(\frac{\partial^2\rho}{\partial z^2}\right)_{zo} \end{bmatrix} \quad (3)$$

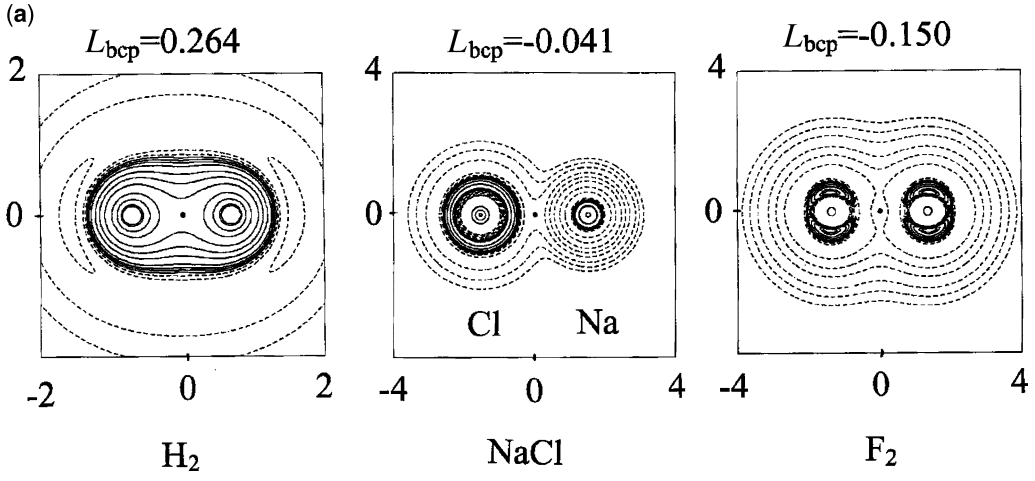

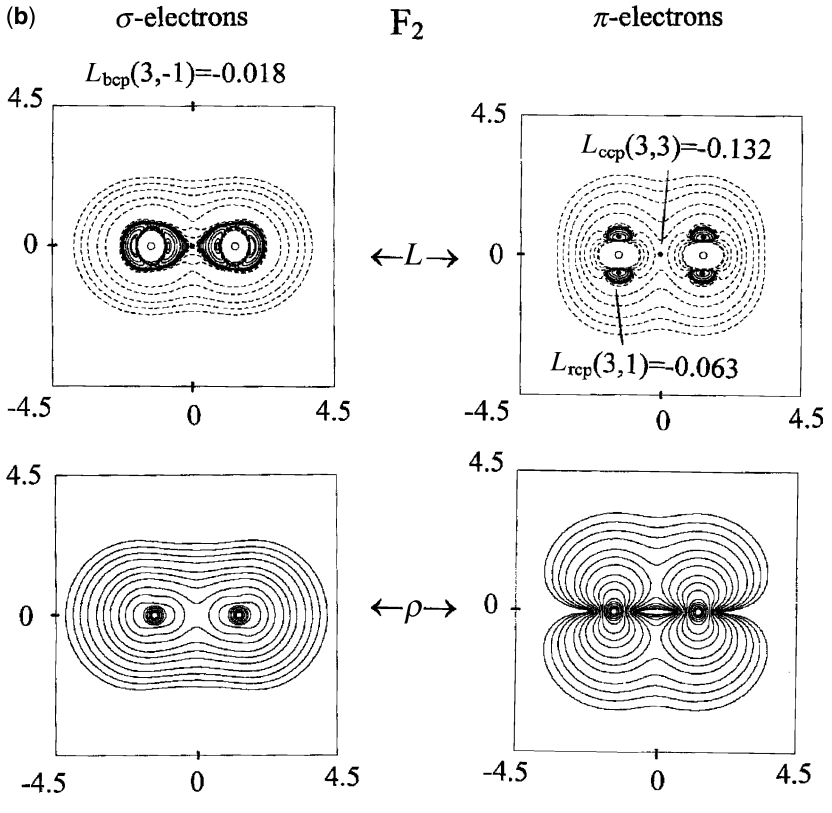

Their components can easily be calculated from the knowledge of the density $\rho(\vec{\mathbf{r}})$ on a 3D grid, as available from most quantum chemistry codes.

The topological analysis of $(\overrightarrow{\nabla\boldsymbol{\rho}})_{\mathbf{r0}}$ makes it possible to locate stationary points in ρ which might correspond to local minima, maxima, or saddle points. They further allow to identify atoms or fragments of atoms in a molecule or atomic subspaces bordered by surfaces S (basins) on which the flux of the gradient vanishes (Eq. (4)) where $(\overrightarrow{\nabla\boldsymbol{\rho}})_S$ is calculated at each point of the surface, $\overrightarrow{\mathbf{n}_S}$ is any vector perpendicular to the surface.

$$(\overrightarrow{\nabla\boldsymbol{\rho}})_S \cdot \overrightarrow{\mathbf{n}_S} = 0 \tag{4}$$

It has been shown that the virial theorem holds for these basins and integration of ρ over them allows to get atomic or fragment charges within the molecule. The matrix $(\mathbf{H})_{\mathbf{ro}}$ allows to calculate the Laplacian of the electron density as a sum of its diagonal elements (Eq. (5)), which is invariant with respect to the choice of the coordinate system.

$$L = -\frac{1}{2}\left(\frac{\partial^2\rho}{\partial x^2}\right)_{x_o} + \frac{1}{2}\left(\frac{\partial^2\rho}{\partial y^2}\right)_{y_o} + \frac{1}{2}\left(\frac{\partial^2\rho}{\partial z^2}\right)_{z_o} \tag{5}$$

Diagonalization of the matrix H, leading to principle curvatures as the eigenvalues and principal axis as the eigenvectors allows to explore the topology of the electron density at any given point of space. The values of these quantities at the points where $(\overrightarrow{\nabla\boldsymbol{\rho}})$ vanishes (critical points) are of particular interest. They are usually denoted by (r, s), with r standing for the rank (number of non-zero eigenvalues) and s for the signature (sum of signs of the eigenvalues). Bond critical points, denoted as (3, −1) are such, where two eigenvalues are negative, while one is positive corresponding to (two) maxima and one minimum with respect to the directions defined by the eigenvectors. The eigenvector for the positive eigenvalue connects two atoms and defines a bond path between them. Positions of the nuclei are characterized by a maximum of ρ [(3, −3) critical points, or nuclear attractors]. Furthermore one finds ring and cage critical points where two or three eigenvalues (curvatures) of H are positive, (3, 1) and (3, 3); examples are given by cyclic (cyclopropane) and cage shaped (P_4) molecules, respectively. It has been shown that the values of L at each point (Eq. (5)) can be related with the kinetic $G(\mathbf{r})$ and with the potential $V(\mathbf{r})$ energy density at that point (Eq. (6)) where positive and negative values of (L) characterize regions in space in which charge is accumulated or depleted, respectively.

$$2G(\overrightarrow{\mathbf{r}}) + V(\overrightarrow{\mathbf{r}}) = -L(\overrightarrow{\mathbf{r}}) \tag{6}$$

In Fig. 2 we show three typical examples, two for one electron pair bonding (H_2 and F_2) and one for a typical ionic molecule as NaCl. As expected, electronic charge concentration and depletion between the nuclei of H_2 and NaCl is observed. However, for F_2 we don't see any increase of L between the nuclei. As has been pointed out by *Cremer* and *Kraka* for F_2 [18], L is negative at the bond critical point r_c (−2.908 e.Å^{-5}), but still, the sum of $G(r_c) + V(r_c)$(=2.247–4.292 = −2.045 Hartree. Å^{-3}) results in a negative value of the total energy density ($E = G + V$). The unusual bonding in F_2 has been explained by VB-theory [19] in terms of a very strong mixing between covalent and ionic resonance structures due to a large and

negative resonance integral β in which the kinetic energy term dominates [20]. This has been called a ''charge shift bonding'' [19]. It is interesting and important to note that $(-L)$ can still reflect these results when decomposed into contributions from σ and π character – $[-L(\sigma)]$ and $[-L(\pi)]$, respectively. Figure 2b nicely shows this; thus the plot of $[-L(\sigma)]$ displays two electron pairs between the F nuclei, each belonging to its closest nuclei but with a clear deformation oriented toward the neighbouring nucleus. Also the σ-lone pairs are clearly discerned, as well as the π-oriented lone pairs on F, which now, due to the *Pauli*-repulsion are oriented in a direction outwards the F–F bond axis.

The distinction between orbitaly resolved contributions in L and in ELF (see next section) plays a central role in our analysis of the TM–ligand bond as we shall see in Section III.

Finally, it is worth mentioning that the electron pair density in conjunction with the AIM theory enables one to determine the average number of electron pairs that are localized to each atom (A) and the number that are formed between any given pair of atoms A and B. Within this quantitative AIM framework [21] atomic localization and delocalization indices noted $\lambda(A)$ and $\delta(A, B)$ have been defined, the latter being sometimes referred to as bond orders. Applications of this approach to characterize metal–ligand bonding in TM di- and tri-halides have already been reported [22].

II.2.2. The Electron Localization Function (ELF)

The introduction of the electron localization function (ELF) by *Becke* and *Edgecombe* in 1990 [12] has lead to a quantitative index to describe intuitive concepts like chemical bond and electron pair. This function allows to describe in a topological way a quantity related to the *Pauli* exclusion principle. The local maxima of this function define 'localization domains' of which there are only three basic types: valence domains (bonding, non-bonding) and core domains (see below). The spatial organization of localization domains provides a basis for a well-defined classification of bonds. An obvious advantage of this function is that it can be derived from computed and experimental electron densities.

The electron localization function has been originally derived from the conditional probability of finding an electron of spin σ at $\mathbf{r}'$ when an electron with the same spin is located at $\vec{\mathbf{r}}$. As proposed by *Becke* and *Edgecombe*, ELF is a simple function taking values between 0 to 1 and measuring the excess local kinetic energy due to the *Pauli* repulsion.

For a single determinental wavefunction built from *Hartree-Fock* or *Kohn-Sham* orbitals φ_i and an electron density ρ_σ the value of ELF is given by Eq. (7) where D_σ and D_σ^0 are described by Eqs. (8) and (9).

$$\mathrm{ELF} = \frac{1}{1 + \left(\frac{D_\sigma}{D_\sigma^0}\right)^2} \tag{7}$$

$$D_\sigma = \sum_{i=1}^{N} |\nabla \varphi_i|^2 - \frac{1}{4}\frac{|\nabla \rho^\sigma|^2}{\rho^\sigma} \tag{8}$$

$$D_\sigma^0 = \frac{3}{5}(6\pi^2)^{2/3}\rho_\sigma^{5/3} \tag{9}$$

In Eqs. (7) and (8) D_σ is the excess local kinetic energy due to *Pauli* repulsion and represents the curvature of the electron pair density for electrons of identical σ spins (the *Fermi* hole) for the actual system. D_σ^0 is the analogous quantity for a homogeneous electron gas with the same density at point of space $\mathbf{r}$ ($\rho(\mathbf{r})$). D_σ is a positive quantity which is small in regions of space where the electrons do not experience the *Pauli* repulsion, that is, where electrons are alone or form pairs with anti parallel spins (bosons). It is also small if pairs of parallel spin electrons are far away from each other and large if they are close in space.

ELF can be calculated from the known ρ_σ on a grid in the three-dimensional space. Usually the quantum chemical calculations give results that are non-local quantitative, predictive, and method dependent. In the discussion of the chemical bonds, chemists use arguments that are local, qualitative, explicative, and approximation independent. ELF fills the gap between these approaches by providing a mathematical definition of the bond as a local property of matter. Furthermore since quantum mechanics is valid by definition, the property can be obtained from theory and from experiment and moreover is close to the *Lewis* nomenclature. One main advantage is the independance from the approximation level of theory.

ELF can take values between 0 and 1. For regions where there is no localization of electron pairs or regions where electron of the same spin are predominant, ELF has a value close to 0. For regions where there is a high pair localization and also in region dominated by a single, localized electron, ELF is close to 1. For a value of ELF = 0.5, the region is exactly of electron-gas type.

Topological analysis of ELF by *Savin* and *Silvi* [13, 16a–16c] allow to locate critical points (m) in space, where ∇ELF(r) is zero and which are characterized by their index I(m) – the number of positive eigenvalues of the second derivative matrix. Critical points of index 0 and the manifold of points confined to them define an attractor (local maximum) and the basin of an attactor, respectively. Critical points of index larger than 0 is a separatrix: it is a boundary between basins. There are two types of basins – core and valence ones. The structure given by the core basins closely resembles the inner atomic structure. The valence basins are characterized by their synaptic order – the number of cores to which they are connected. Any subset of the molecular space bounded by an external closed isosurface ELF(r) = f is a domain; for each point of this subset the inequality ELF(r) > f holds. For any system there exist low values of ELF(r) = f defining an unique composite parent domain. If one increases the values of f of an isosurface of ELF its topology may change dramatically at some critical (threshold) values – a reducible (composite) domain splits into several domains each containing fewer attractors than the parent domain. This reduction appears at turning points of index 1 located on the separatrix of two basins involved in the parent domain. Ordering of these turning points (localization nodes) by increasing f generates tree (bifurcation) diagrams reflecting the hierarchy of the core and valence basins in an order of increasing localization (ELF values). In a molecule for example, the initial parent domain first splits into core domains and a single valence domain which contains all valence attractors with as many holes inside as there are atomic cores in the molecule. A given core contributes by one to the synaptic order of an adjacent

valence basin. The partition of reducible domains into core and valence domains is called core/valence bifurcation. It can occur in two different ways: either the core irreducible domains split before the valence ones, or the core/valence separation takes place after the valence division into two or more domains. While the first process is characteristic for molecules or molecular ions, the second one is characteristic for weak interactions among fragments. An ELF study on VO_x^+ and VO_x ($x = 1$–4) clusters based on the analysis of the bifurcation of the localization domains [23] provides a valuable information about the V–O bond and will be discussed in the context of our results in Section III.3.

We can conclude, that the topological analysis of the gradient field of ELF provides a framework for the partition of the molecular space into basins of attractors having a clear chemical meaning. While basin populations are evaluated by integrating the one-electron density over basins, the variance of the basin populations provides a measure of the delocalization. An application of this approach to study geometries of formally d^0 MX_n ($X = F,H,CH_3$, and O; $M = Ca$ to Mn, $n = 2$–6) contributes to understanding of their non-VSEPR geometries [24]. An overview of the possibilities offered by the topological analysis of ELF ranging from isolated atoms to solids may be found elsewhere [13, 22, 25].

We should finally note, that applications of AIM and ELF gain interpretative power when separated into components of different symmetry. It has been shown, for example, that the separation of ELF into its σ and π-components in aromatic molecules allows to quantify the concept of resonance and to set up a scale for aromaticity [26]. A possible justification of this approach could be done by re-expressing ELF in terms of time independent electron transition current densities between occupied orbitals [27].

II.3. Angular Overlap Model [28–31]

The energies of the d-orbitals for complexes with ligand to metal donor acceptor bonds are described by energies for $\lambda = \sigma$ and π-antibonding, which pertain to well aligned metal 3d- and ligand p-orbitals, e_λ. Using perturbation theory and the *Wolfsberg-Helmholz* approximation for the resonance integral $H(M\text{-}L)_\lambda$ one obtains Eq. (10) for e_λ, showing a quadratic dependence on the group overlap integral S_λ.

$$e_\lambda \cong \frac{H(M-L)_\lambda^2}{H_M - H_L} \approx \frac{H_L^2}{H_M - H_L} \cdot S_\lambda^2 \tag{10}$$

e_λ parameters can be obtained using spectral information from a fit of ligand field expressions. For an octahedral complex only one ligand field splitting parameter (Eq. (11)) can be derived which do not allow to separate e_σ and e_π.

$$10\mathrm{Dq} = 3e_\sigma - 4e_\pi \tag{11}$$

This situation changes when going to symmetric complexes. Figure 3 illustrates this for a square-pyramidal ML_5 complex where also AOM expressions for the energies of the d-orbitals are given. For a non centro-symmetric complex a mixing of $|s\rangle$ and $|p\rangle$ into the $|d\rangle$ orbitals of the TM is possible. This is particularly pronounced for the $d_{z2\text{-}4s}$ mixing that leads to lowering of the d_{z2} orbital in energy,

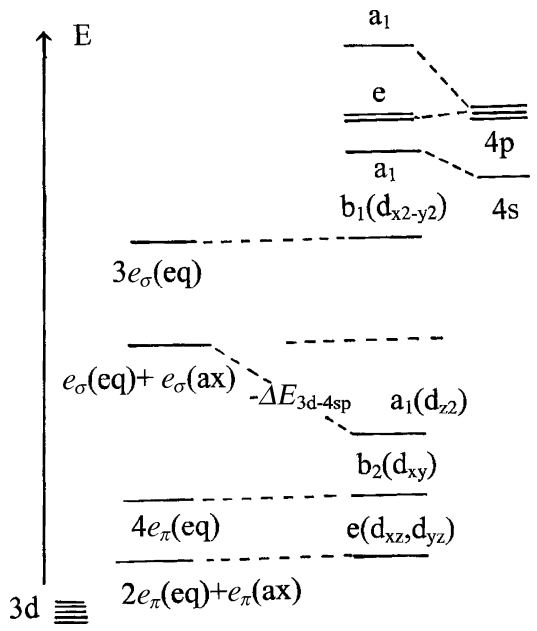

Fig. 3. Splitting of the d-orbitals in a quadratic pyramidal TM complex with five ligands – four equatorial, one axial; parameterization of these energies in terms of the angular overlap model without (left) and with 3d-4s, 4p mixing (right) is given along with the unperturbed 3d (left) and 4s, 4p (right) orbitals; e_σ(ax), e_π(ax) and e_σ(eq), e_π(eq) pertain to antibonding energies due to the axial and equatorial ligands, respectively, and $\Delta E_{3d\text{-}4sp}$ energies reflect the stabilization of the $3d_{z2}$ orbital by mixing with mostly (4s) and to lesser extent with the (4p) orbital; the lowering of energy of the e(d_{xz},d_{yz}) orbital due to mixing with the $4p_x$, $4p_y$ functions is neglected; these equations have been used to deduce AOM parameters e_σ and e_π from KS-DFT calculations on the ground state of $Cr^{III}X_5$ ($X = H_2O$,F,Cl,Br,I) (Table 5) with *all* Cr-*X* bond lengths taken to be the same as those for the corresponding octahedral $Cr^{III}X_6$ species

which is described by an additional parameter $\Delta E_{3d\text{-}4sp}$ and which is known to become mostly non-bonding in the limiting case of a square-planar complex [32–33]. DFT calculations enable to use *Kohn-Sham* orbital energies to get values of $3e_\sigma$,e_π and $\Delta E_{3d\text{-}4sp}$, and to compare these with the results obtained from ETS bonding analysis, pertaining to all occupied orbitals. Thus a clear distinction between bonding and antibonding contributions becomes possible and will be discussed together with the analysis based on the electron density (Laplacian and ELF).

II.4. Computational Details

DFT calculations and bonding analysis in this work have been performed using the Amsterdam Density Functional (ADF) program [10] (release 2004.01) using the *Perdew-Wang* (*PW*91) gradient corrected functional. Triple zeta basis sets (TZP) as provided by the program data base have been taken for the calculations. Geometry optimizations allowing to fix the geometry of every complex have been carried out using the LDA implemented in the VWN-functional. This procedures are known to yield TM–ligand bond distances in good agreement with experiments.

The octahedral $M^{III}X_6^{3-}$ complexes studied in this work are highly negative charged. One may ask how bonding is affected by a charge compensating medium

(solvent in solutions or counter ions in the solid). To mimic this effect and study its influence on the bonding and ligand field parameters we have chosen $CrCl_6^{3-}$ as an example and used the conductor-like screening model (COSMO [34]) as implemented in ADF [35]. Solvent radii of 1.75 and 0.97 Å have been selected for Cl and Cr. The dielectric constant and the solvent radius ε has been fixed at 78.4 and 1.4 Å, respectively (pertaining to water as a solvent) [36].

Topological analyses of the electron density have been made using two home made programs written in Matlab: one for *Bader* analysis (Emma1) and another one (Emma2) for ELF calculations [37]. Both programs are interfaced with the ADF program package and make use of the tape21 file and the "densf" utility program, the latter providing the electron density on a grid.

To calculate the orbitally resolved Laplacian and ELF values we utilized the high symmetry of the systems and used non-zero electronic ground state occupations, taking SCF *Kohn-Sham* orbitals of a given symmetry, while ignoring all orbitals of a different symmetry (by setting zero occupation numbers in the input).

III. Results and Discussions

III.1. Complexes with CN=6

III.1.1. Halide Complexes of Cr^{III}, Co^{III}, Mo^{III}, W^{III}

MO energy diagrams for the bare $Cr^{III}X_6^{3-}$ (d^3, $^4A_{2g}$ ground state, $X = F^-, Cl^- Br^-$ – Fig. 4) anions show the pattern for an octahedral complex, with bonding a_{1g}, e_g, t_{2g}, and t_{1u} MOs that are dominated by ligand and antibonding MOs dominated by

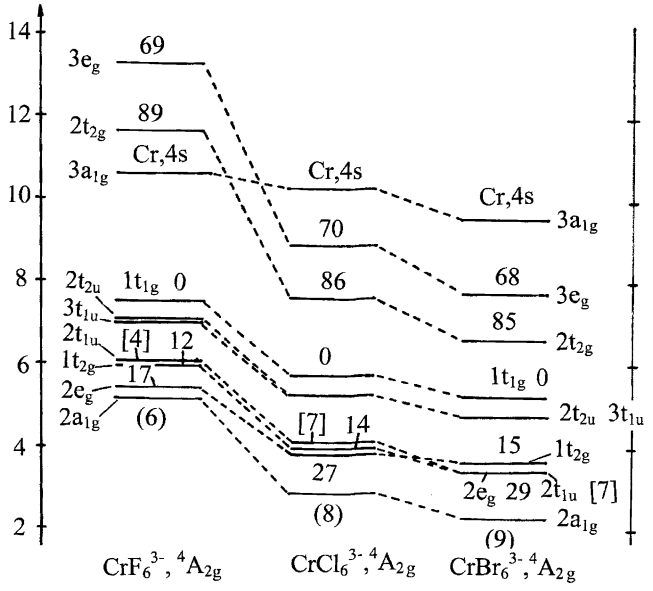

Fig. 4. *KS*-MO energy (in eV) diagram for CrX_6^{3-} (X = F,Cl,Br) charge uncompensated species; contributions (in percentages) from the Cr 3d, 4s (in "( )" brackets) and 4p (in square "[ ]" brackets) are given

metal orbitals, *i.e.*, typical for ligand to metal donor–acceptor bonds. It can be qualitatively understood by the following expressions for the stabilization/destabilization of the ligand/metal orbitals obtained from the angular overlap model (Eq. (12a)) and the qualitative order for the magnitude of the AOM parameters as given by Eq. (12b).

$$\begin{aligned}\delta E(\mathrm{a_{1g}}) &= \pm[6e_\sigma(4\mathrm{s})]\\ \delta E(\mathrm{t_{1u}}) &= \pm[2e_\sigma(4\mathrm{p}) + 4e_\pi(4\mathrm{p})]\\ \delta E(\mathrm{e_g}) &= \pm[3e_\sigma(3\mathrm{d})]\\ \delta E(\mathrm{t_{2g}}) &= \pm[4e_\pi(3\mathrm{d})]\end{aligned} \tag{12a}$$

$$e_\pi(4\mathrm{p}), e_\sigma(4\mathrm{p}) < e_\sigma(4\mathrm{s}) < e_\pi(3\mathrm{d}) < e_\sigma(3\mathrm{d}) \tag{12b}$$

Mixing between metal and ligand orbitals is largest for the metal 3d- and much smaller, but not negligible for the metal 4s- and 4p-orbitals. The participation of the $|4\mathrm{s}\rangle$ and $|4\mathrm{p}\rangle$ orbitals to bonding increases when going from F to Cl to Br complexes, which is generally fulfilled also for the other coordination numbers with the same ligands (see below). For CrF_6^{3-} we notice the anomalous position of the $3a_{1g}(4s)$ MO, being found below the $2t_{2g}$ and $3e_g$ MOs. This is clearly an artifact connected with the choice of the orbital exponent and possibly the additional effect of the uncompensated high negative charge of the anion. Going to Cl and Br, the correct ordering $2t_{2g} < 3e_g < 3a_{1g}$ is restored, but still, the position of $3a_{1g}(4s)$ is far too low. Thus, for free Cr^{3+} we calculate $|4\mathrm{s}\rangle$ as lying 11 eV above the $|3\mathrm{d}\rangle$ orbitals. To compensate for the negative cluster charge, COSMO calculations for $CrX_6^{3-}(X = \mathrm{F,Cl})$ have been performed. Their MO diagrams are compared with those of the bare anions in Fig. 5. The contribution of a charge compensating solvent

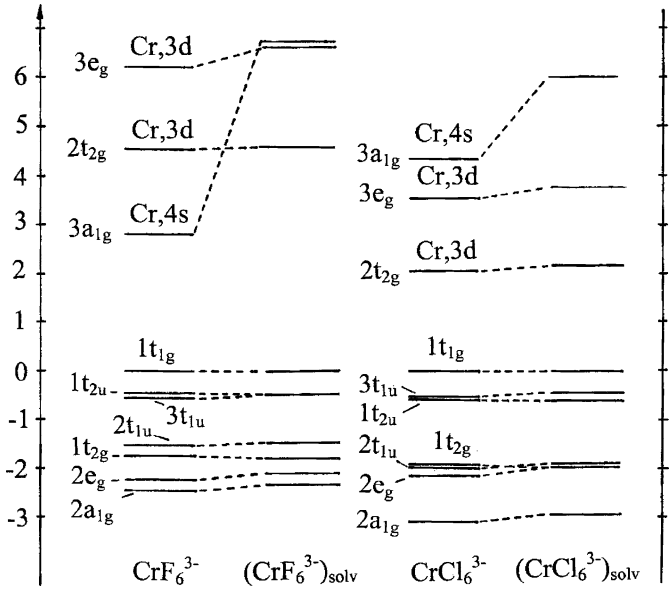

Fig. 5. The effect of charge compensating solvent continuum on the KS-MO energies (right) in comparison with those calculated using bare anions (left) for CrF_6^{3-} and $CrCl_6^{3-}$ as studied using a COSMO model with solvent parameters taken for water (see text)

Table 2. Energy partitioning analysis of octahedral M(III) hexahalides ($M = $ Cr, $X = $ F,Cl,Br,I), $MoCl_6^{3-}$, and WCl_6^{3-} (from ionic (M^{3+}, X_6^{6-})[c] reference fragments, energies in eV)[a], optimized M-X bond distances (R in Å)[b], *Mulliken* charges (q_M, q_X), and estimated and experimental values (in square brackets) for the ligand field splitting parameter 10Dq; percentages of ΔE_{Elstat} and ΔE_{orb} to the total attractive energy $E_{\text{Elstat}} + E_{\text{orb}}$ along with contributions from orbitals of different symmetry to E_{orb} are given in parenthesis

MX_6^{3-}	CrF_6^{3-}	$CrCl_6^{3-}$	$CrBr_6^{3-}$	$MoCl_6^{3-}$	WCl_6^{3-}	
					non-relat.	relat. ZORA
R	1.964	2.397	2.562	2.511	2.510	2.545
q_M	1.51	0.47	0.46	0.79	1.11	1.14
q_x	−0.75	−0.58	−0.58	−0.63	−0.69	−0.69
$10Dq \cong e(e) - e(t_2)$	1.58 [1.88]	1.34 [1.59]	1.19 [-]	1.72 [2.38]	1.96 [-]	1.81 [-]
ΔE_{Prep}	93.20	83.13	71.47	77.74	77.34	78.85
ΔE_{int}	−124.13	−107.22	−100.52	−103.34	−101.36	−101.85
ΔE_{Pauli}	10.57	9.49	8.32	13.58	17.99	15.65
ΔE_{Elstat}	−107.62 (80)	−87.72 (75)	−76.69 (70)	−88.36 (76)	−89.70 (75)	−88.79 (76)
ΔE_{orb}	−27.07 (20)	−29.00 (25)	−32.15 (30)	−28.57 (24)	−29.65 (25)	−28.71 (24)
$\Delta E_{\text{orb}}(a_{1g})$	−1.77 (6)	−1.97 (7)	−2.25 (7)	−1.62 (6)	−1.73 (6)	−2.82 (10)
$\Delta E_{\text{orb}}(e_g)$	−17.51 (65)	−13.18 (45)	−11.81 (37)	−17.26 (60)	−18.67 (63)	−17.90 (62)
$\Delta E_{\text{orb}}(t_{1g})$	−0.58 (2)	−0.96 (3)	−0.93 (3)	−0.84 (3)	−0.93 (3)	−0.88 (3)
$\Delta E_{\text{orb}}(t_{2g})$	−0.50 (2)	−7.04 (24)	−10.33 (32)	−4.32 (15)	−3.04 (10)	−1.52 (5)
$\Delta E_{\text{orb}}(t_{2u})$	−0.67 (2)	−0.93 (3)	−1.04 (3)	−0.80 (3)	−0.89 (3)	−0.83 (3)
$\Delta E_{\text{orb}}(t_{1u})$	−6.04 (22)	−4.92 (17)	−5.78 (18)	−3.72 (13)	−4.39 (15)	−4.76 (16)

[a] $M_s = 3/2$ spin-unrestricted, basis: TZP, non-relativistic, frozen cores: Cr,Mo,W up to 3p,4p,4f, X: up to 1s(F), 2p(Cl), 3d(Br), 4d(I), *PW*91 functional; [b] $M_s = 3/2$ spin-unrestricted, LDA functional; [c] electronic configurations of the chosen reference fragments are: $M^{3+}(d^3)$, $X_6^{6-}(a_{1g}^2 t_{1u}^6 e_g^4 a_{1g}^2 t_{1u}^6 t_{2g}^6 e_g^4 t_{2u}^6 t_{1u}^6 t_{1g}^6)$

modifies considerably the orbital levels; the energy of the orbital $3a_{1g}$ increases significantly. Also, the $3e_g$-$2t_{2g}$ energy gap – which is a measure of the cubic ligand field splitting 10Dq (Eq. (11)) increases and improves the agreement with experiment (Table 2). A MO diagram (Fig. 6) for the series MCl_6^{3-}($M = $ Cr,Mo,W) clearly shows variations of the bonding scheme across the series; the covalent mixing between metal and ligand orbitals increases when going from Cr to Mo. However, because of the increased relativistic effects observed for W, the transition from Mo^{III} to W^{III} does thus not show a monotonic variation.

Ligand field spectroscopy allows to characterise all these complexes as being mainly ionic. Table 2 includes the results from an energy decomposition analysis, with M^{III} and X_6^{6-} as reference fragments. In choosing such fragments, we exclude X–X interactions, thus focusing on pure TM–ligand bonding. To prepare such fragments, a large amount of energy ΔE_{Prep} is required. It includes the energies for the $M \rightarrow M^{3+} + 3e^-$ and the $X^- \rightarrow X + 1e$ ionization (a negative sign denotes the electronic affinity) and the additional repulsive energy needed to bring $6F^-$ from infinity to their actual positions in the complex. $M^{3+} - X_6^{6-}$ interaction energies ΔE_{int} are strongly negative and are dominated by the classical electrostatic term (ΔE_{Elstat}) as expected. However, ΔE_{orb} terms reflect the metal–ligand covalency as well as polarization and they show that these effects are very significant. Their relative importance to the total attractive energy $\Delta E_{\text{Elstat}} + \Delta E_{\text{orb}}$ increases from F to Cl to Br: 20,

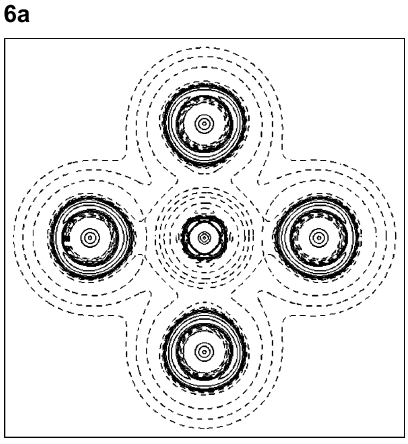

Fig. 6. Contour plots for the Laplacian of the electron density (a) and electronic localization function (b) pertaining to the total electron density of the bare $CrCl_6^{3-}$ complex in one of the planes containing Cr^{3+} and four Cl^- ligands; for contour values of the Laplacian see Fig. caption 2; the overall pattern of the two plots display a mostly ionic bonding without charge concentration between Cr and Cl; contour plots for solvated species are very similar reflecting a slight decrease of Cr–Cl bond distances in the case of solvent

25, and 30% for the covalency and −27.07, −29.00 and −32.15 eV for the magnitude, respectively. This is consistent with the chemical intuition: *i.e.*, increase of the Cr–*X* covalency when going from F to Cl to Br. A closer look at the orbital decomposition of ΔE_{orb}, shows however, that contributions from $|4s\rangle$ and $|3d\rangle$ orbitals to σ bonding (reflected by the a_{1g} and e_g energy terms), $\sigma + \pi$ bonding (t_{1u}), and π-bonding (t_{2g}) behave in a different way across the {F,Cl,Br} series. The e_g and t_{1u} energies decrease, while the energies of t_{2g}, and a_{1g} increase in this order. Thus, the trend observed in ΔE_{orb} is the result of a subtle balance between contributions from different bonding interactions. The behaviour of the e_g and t_{2g} orbitals also explains the lowering of 10Dq when going from F to Br as a result of the decreasing e_g-σ antibonding interaction. The account for solvation shows a strong stabilization of the anion due to solute–solvent interactions which are larger for F^-, than for Cl^-. However, only the metal (3d)-ligand σ-bonding is stabilized by the solvent. Table 3, where the various contributions of the components obtained in the energy decomposition are listed, clearly shows this. Contributions from orbitals other than from e_g are positive and do sum up to yield a small, yet, positive value of $\delta\Delta E_{\mathrm{orb}}$.

The results from our ETS analysis are strongly supported by the Laplacian of the electron density and the ELF functions. The plots of these functions obtained from the total density do not show any accumulation of charge between the TM and the ligand. This is seen from Fig. 6 where contour plots for (*L*) and ELF for $CrCl_6^{3-}$ are displayed. The overall features of both plots reflect a mostly ionic bond, with charge depletion between the metal and the ligand. It might still lead to negative total energy densities at the bond critical points, however (see Section II and Ref. [18]). The situation changes if one considers the Laplacian of the density plot resolved into orbital contributions instead. Figures 7a and 7b illustrate this for the σ-bonds due to the a_{1g} and the e_g orbitals, respectively. Accumulation of electronic charge into regions of space between Cr and Cl is clearly stronger for e_g and

Table 3. Changes of ΔE_{orb} and of its components of different symmetry going from bare CrF_6^{3-} and $CrCl_6^{6-}$ to solvated species ($\delta\Delta E_{orb}$); solute–solvent interaction energies for hydrated species (E_{solv}) and changes of the values of 10Dq (δ(10Dq), all energies in eV) and of the Cr–F and Cr–Cl optimized bond lengths (δR, in Å) are also included

Changes $(CrX_6^{3-})_{bare} \rightarrow (CrX_6^{3-})_{solv}$	$X=$ F	Cl
$\delta\Delta E_{orb}$	0.259	0.294
$\delta\Delta E_{orb}(a_{1g})$	0.100	0.158
$\delta\Delta E_{orb}(e_g)$	−0.779	−0.797
$\delta\Delta E_{orb}(t_{1g})$	0.285	0.197
$\delta\Delta E_{orb}(t_{2g})$	0.072	−0.026
$\delta\Delta E_{orb}(t_{2u})$	0.281	0.224
$\delta\Delta E_{orb}(t_{1u})$	0.328	0.539
E_{solv}	−21.520	−17.598
δ(10Dq)	0.355	0.112
δR	−0.06	−0.06

weaker for a_{1g}. Also the presence on lone pairs densities on the ligands in regions of space opposite to the metal–ligand bond direction is obvious. These features become even more pronounced when looking at the ELF plots. In Figs. 8a and 8b we compare contours for ELF resolved into $\sigma(e_g)$ and $\pi(t_{2g})$, respectively. It follows, that localization valence domains are much more pronounced for the σ-density, when compared to the π-density. They are shifted from the midpoint of the Cr–Cl bond vector toward the ligand in agreement with electronegativity

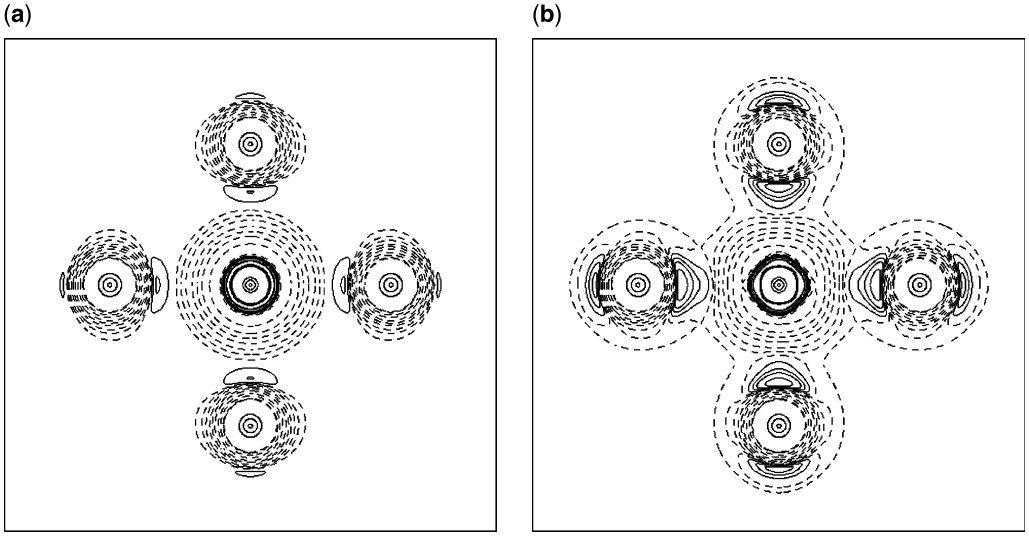

Fig. 7. Contour plots for the Laplacian of the electron density using σ densities resolved into a_{1g} (a) and e_g (b) symmetry components; plots are given for one of the planes containing Cr^{3+} and four Cl^- ligands and values of the Laplacian for the contour lines are the same as specified in Fig. caption 2; solid lines depict charge concentrations into bonding (between Cr and Cl) and lone-pair domains, which are more pronounced for the e_g electron density and less pronounced, yet clearly discernible for the a_{1g} electron density

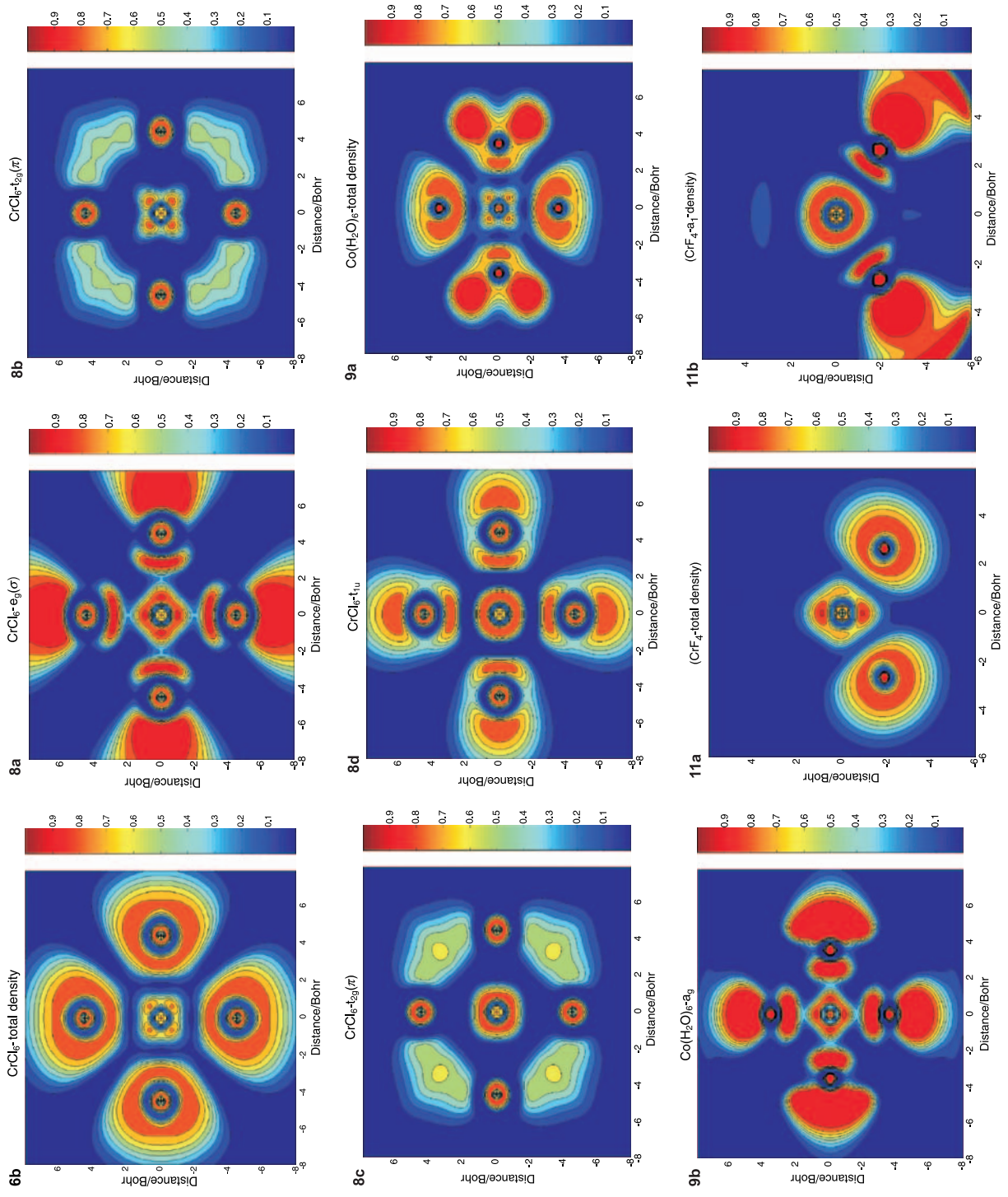
6b
CrCl6- total density
8b
CrCl6-t2g(π)
11b
(CrF4-a1-density)
8a
CrCl6- eg(σ)
8d
CrCl6-t1u
11a
(CrF4-total density)
8c
CrCl6-t2g(π)
9b
Co(H2O)6-ag
9a
Co(H2O)6-total density
Distance/Bohr
Distance/Bohr

considerations. It should be pointed out, however, that Cr–Cl π-bonding is weakened by admixture of the antibonding $(2t_{2g})^3$ configuration. Figure 8c exhibits this behavior in an impressive way: when constructing this plot, the three d-electrons on the antibonding $2t_{2g}$ MO have been removed and the picture reflects the effect of the π-bonding electrons only. Finally, Fig. 8d illustrates that valence $|4p\rangle$ orbitals can not be neglected in the discussion of the TM–ligand bond. This is in agreement with the energy decomposition analysis, which tends to show that for $CrCl_6^{3-}$, $|4p\rangle$ orbitals seem to participate to bonding even stronger than $|4s\rangle$ ones.

III.1.2. Aquo-Complexes of Cr^{III} and Co^{III}

Water is considered to form highly anisotropic π-bonds with transition metals such as $Ti^{III}(d^1)$, $V^{III}(d^2)$, and Mn^{III}(high-spin d^4) as this is convincingly shown by EPR and electronic *Raman* studies of the corresponding complexes [38–40]. However, analysis of bonding in these complexes is complicated by the presence of *Jahn-Teller* effect. The ground states are orbitally degenerate – $^2T_2(d^1)$, $^3T_1(d^2)$, and $^4E(d^4)$, respectively, and these studies mostly focused on this effect. To characterize TM–H_2O bonds, we have chosen $Cr(H_2O)_6^{3+}$ with $|(2t_{2g})^3, {}^4A_{2g}\rangle$, and $Co(H_2O)_6^{3+}$ with $|(2t_{2g})^6, {}^1A_{1g}\rangle$ ground state as test cases. Energy decomposition analyses have been carried out for a single H_2O molecule interacting with a $M(H_2O)_5^{3+}$ ($M = Cr^{3+}, Co^{3+}$) fragment (Table 4). In agreement with the lowering of M–O bond length when going from left to right in the TM series, the total bond energy of one H_2O is larger for Co than for Cr. The bonding interaction is dominated mostly by the electrostatic term ΔE_{Elstat}, but orbital interaction is found to play an important role as well. Covalent bonding terms are calculated to be much stronger for σ than for π interactions, as expected. In agreement with the smaller number of electrons occupying the antibonding $3d_\pi$ orbitals (3 for Cr and 6 for Co) and in spite of the lower bond distance for Co, π-bonding energy for Cr–OH_2 is found to be about two times larger than for Co–OH_2. It is very surprising that

Fig. 8. The electronic localization function for $CrCl_6^{3-}$ in one of the planes containing Cr^{3+} and four Cl^- ligands constructed partitioning the electron density into e_g, Cr(3d)–Cl σ (a), t_{2g}, Cr(3d)–Cl π (b, c), and t_{1u}, Cr(4p)–Cl $\sigma + \pi$ (d) components; the contour plots for the t_{2g} density (b, c) reflects the weakening effect on the Cr–Cl bond caused by the three antibonding t_{2g}(3d) electrons, which have been accounted for in the plot (b) but ignored in the plot (c)

Fig. 9. Electronic localization function for $Co(H_2O)_6^{3+}$ with a T_h geometry (treated in its D_{2h} subgroup by ADF); contour plots are based on the total electron density in (a) and on its a_g symmetry component in (b); the irreducible representations (irreps) spanned by the valence orbitals of the transition metals give rise to the following irreps of the D_{2h} subgroup: $e_g(d_{z2}, d_{x2-y2}) \rightarrow a_g(d_{z2}, d_{x2-y2})$, $t_g(d_{xy}, d_{xz}, d_{yz}) \rightarrow b_{1g}(d_{xy}), b_{2g}(d_{xz}), b_{3g}(d_{yz})$; $a_g(4s) \rightarrow a_g$, $t_u(4p_x, 4p_y, 4p_z) \rightarrow b_{1u}(4p_x), b_{2u}(4p_y), b_{3u}(4p_x)$; thus the plot in (b) reflects the combination of bonding effects with participation of the d_{z2}, d_{x2-y2}, and 4s valence orbitals of the TM

Fig. 11. Contour plots for the electron localization function of CrF_4 with a T_d geometry within a plain containing a CrF_2 molecular fragments constructed using the total electron density (a) and its partitioning into a_1 (b), t_2 (c), and e (d) symmetries; the plots reflect the participation of the Cr 4s σ (a_1), 3d and 4p $\sigma + \pi$ (t_2), and 3d π (e) to the Cr–F bonding in (b), (c), and (d), respectively

Table 4. Energy partitioning analysis for octahedral Cr(III) and Co(III) hexa-aquo complexes calculated starting from $M(H_2O)_5^{2+}$ ($M = Cr^{III}$, $d^3(t_{2g}^3)$ and Co^{III}, $d^6(t_{2g}^6)$) complex units with the octahedral bond distances and bond angles and adding a sixth H_2O ligand to complete the coordination sphere to the octahedron; deduced values of the AOM parameters e_σ, $e_{\pi s}$($\perp$ H_2O plane), and $e_{\pi c}$(|| H_2O plane) are also given; energy values are listed in eV[a], optimized Cr(Co)–OH_2 bond distances (R) in Å[b]

$M(H_2O)_6^{3+}$	$M =$	Cr^{III}	Co^{III}
R		1.971	1.888
ΔE_{Pauli}		2.583	3.140
ΔE_{Elstat}		−2.985	−3.481
ΔE_{orb}		−2.224	−2.521
ΔE_{int}		−2.627	−2.862
$\Delta E_{\text{orb}}(a_1)$ σ		−1.397	−2.005
$\Delta E_{\text{orb}}(b_1, xz, \pi\perp H_2O\text{-plane})$		−0.512	−0.245
$\Delta E_{\text{orb}}(b_2, yz, \pi\|\|H_2O\text{-plane})$		−0.306	−0.265
e_σ		1.277	1.331
$e_{\pi s}(\perp H_2O$ plane)		0.448	0.614
$e_{\pi c}(\|\| H_2O$ plane)		0.070	0.018
$10Dq = 3e_\sigma - 2e_{\pi s} - e_{\pi c}$		2.795	2.729

[a] Spin-restricted calculation, basis: TZP, non-relativistic, frozen cores: Cr(Co) up to 3p, O: up to 1s, *PW*91 functional; [b] spin-restricted, LDA functional

π-anisotropy is not very pronounced, when comparing π-bonding energies within (b_2) and out of (b_1) the TM–OH_2 plane. Only for Cr(III) we do observe $|\Delta E_{\text{orb}}(b_1)| > |\Delta E_{\text{orb}}(b_2)|$. Apparently, when considering bonding energies, π-anisotropy does not show up in our analysis.

Using the energies of the *Kohn-Sham* orbitals with dominant metal character of the fivefold coordinated fragments (see Fig. 3) we could estimate the corresponding AOM-parameters which are listed in Table 4. The values obtained for $e_{\pi s}$ and $e_{\pi c}$ are in agreement with the usual assumption made in LF theory, namely, that out-of-plane π-antibonding is larger than in the TM–OH_2 plane. Finally, the variation of the respective e_σ and e_π parameters do compensate in 10Dq leading to values of this latter parameter which are quite close in magnitude for Cr and Co. Using the same approach, *i.e.*, considering $CrX_5^{2-}(X = F,Cl,Br)$ fragments it was possible to calculate AOM parameters for Cr–*X* bonds. All these results are gathered in Table 5 and compared with values obtained from spectral data. There is a good overall agreement between the two sets of data and this shows that DFT calculations do well reproduce the trends observed experimentally.

Finally, the metal–ligand covalency is nicely expressed in the ELF function for $Co(H_2O)_6^{3+}$ (Fig. 9), both are derived from the total density (Fig. 9a) and from its

Table 5. AOM parameters (in eV) from LFDFT analysis and from experiment (in parenthesis, adopted from Refs. [8, 9]) using optical data for hexacoordinate Cr(III) complexes

Ligand	H_2O	F	Cl	Br	I
e_σ	1.23 (0.93)	1.08 (0.92)	0.70 (0.68)	0.61 (0.61)	0.52 (0.53)
e_π	0.26 (0.17)	0.37 (0.21)	0.18 (0.11)	0.15 (0.07)	0.11 (0.07)

$a_1(\sigma)$ components. The results clearly show the domination of the σ over the π interactions, in full support of our energy decomposition analysis (Table 4).

III.2. Neutral Complexes with CN=4 – Tetrahedral Tetrahalides of Cr^{IV}

The *KS*–MO diagram for the CrX_4 (X = F,Cl,Br,I) series with a $|(2e)^2\ {}^2A_2\rangle$ ground state (Fig. 10) shows the pattern for an tetrahedral complex, with the bonding – $2t_2$, $2a_1$, 1e and the anitibonding 2e, $4t_2$, $3a_1$ (not shown) MOs dominated by ligand (p, s) and metal (3d, 4s) orbitals, respectively. Thus, as in the complexes with CN=6 we have a typical pattern for a ligand-to-metal donor–acceptor bond. In Fig. 10 we also display the fully occupied (by ligand electrons) strictly (t_1) and approximately ($3t_2$) non-bonding MOs. The order of the MOs can qualitatively be understood by the energy decrease/increase of ligand/metal centered orbitals given by the AOM (Eq. (13)) and the inequalities following Eq. (12b).

$$\begin{aligned}
\delta E(a_1) &= \pm[4e_\sigma(4s)] \\
\delta E(e) &= \pm\left[\frac{8}{3}e_\pi(3d)\right] \\
\delta E(t_2) &= \pm\left[\frac{4}{3}e_\sigma(3d) + \frac{8}{9}e_\pi(3d)\right] \\
\delta E(t_2) &= \pm\left[\frac{4}{3}e_\sigma(4p) + \frac{8}{3}e_\pi(4p)\right]
\end{aligned} \tag{13}$$

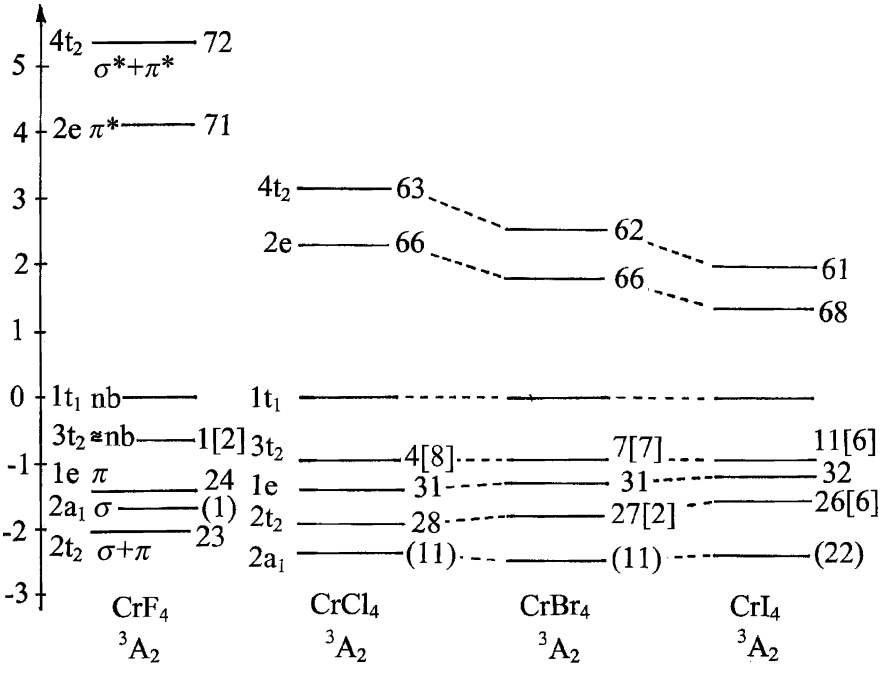

Fig. 10. *KS*-MO diagram for tetrahedral CrX_4 (X = F,Cl,Br,I) molecules in their $|(2e)^2,\ {}^3A_2\rangle$ ground state; percentages of contributions from the 3d, 4s, and 4p orbitals are indicated (without, with "( )", and "[ ]" brackets, respectively)

MO population analyses reflect a very pronounced covalency, which increases when going from the fluoride to the iodide complex. In the same order the participation of $|4s\rangle$ to bonding increases; this is reflected by the contribution of the $|4s\rangle$ atomic orbital to the $2a_1$ MO and its energy lowering when going from CrF_4 to $CrCl_4$. The plot of the ELF using the total electron density for CrF_4 shows a mostly ionic pattern. A similar plot is obtained for the Laplacian of the electron density (Fig. 11a). However, a partitioning of the density into different symmetries shows, for a_1 and t_2, localization of bonding pairs between Cr and F (Figs. 11b, 11c). In spite of the fact that σ- and π-bonding are not separable for T_d it seems that localization of valence domains is mainly due to σ-overlap: the localization of π-bonding pairs (e-symmetry) is not very pronounced (Fig. 11d). In order, not to be biased by the choice of fragments, ETS energy decomposition analyses have been performed using both neutral ($Cr + X_4$) and ionic ($Cr^{4+} + X_4{}^{4-}$) fragments whose results are listed in Table 6. Looking at the $|\Delta E_{\text{orb}}|$ term, we notice that it decreases from the F to I when taking neutral fragments and it increases in that direction for ionic fragments. It is only the latter case which is consistent with the MO diagram (increase of covalency from F to I) as depicted in Fig. 10. Also the electrostatic energy $|\Delta E_{\text{Elstat}}|$ behaves as expected: being largest for CrF_4 and smallest for CrI_4. The trend in the total attractive energy $\Delta E_{\text{orb}} + \Delta E_{\text{Elstat}}$ is finally the one which also determines the behavior of the total bonding energy – decrease of $|\Delta E_{\text{int}}|$ across the $X = \text{F}$ to I series. It is the ΔE_{Elstat} term which dominates this trend. Let us now concentrate on ΔE_{orb} in case of ionic reference fragments. Here the behavior is different to the octahedral complexes: *i.e.*, all of its components, $|\Delta E_{\text{orb}}(a_1)|$, $|\Delta E_{\text{orb}}(e)|$, and $|\Delta E_{\text{orb}}(t_2)|$, increase from F to I (*vide supra*). This is not the case if one starts from neutral reference fragments. In the latter case all these quantities decrease, at variance with the MO scheme (Fig. 10). Focusing again on the $|\Delta E_{\text{orb}}|$ term we observe that this contribution is dominated by $\Delta E_{\text{orb}}(e)$ and $\Delta E_{\text{orb}}(t_2)$, while $\Delta E_{\text{orb}}(a_1)$ should be much smaller. The π bonding energy $\Delta E_{\text{orb}}(e)$ is larger than $\Delta E_{\text{orb}}(t_2)$ ($\sigma + \pi$). This is different from what one expects. Also, the $\Delta E_{\text{orb}}(t_1)$ term should exactly vanish from a bonding point of view. Table 6 shows that this is not the case. As mentioned in Section II, ΔE_{orb} energies reflect not only a stabilization due to covalent bonding, but also pure orbital polarization effects. To suppress the latter effects, we carried out a single zeta (SZ) calculation for CrF_4 whose results are listed in Table 6. Calculations of such a low quality should be avoided, as far as bonding energies are

Fig. 14. The electronic localization for $CrCl_2$, partitioned into components for $\sigma(\sigma_g, \sigma_u)$ bonding in (a) and $\pi(\pi_g, \pi_u)$ bonding in (b)

Fig. 16. Electronic localization function for $Re_2Cl_8{}^{2-}$ taken within a plane containing the Re–Re bond and four Cl ligands belonging to the constituting $ReCl_4{}^-$ fragments; contour diagrams have been plotted using the total density (a), the Re–Re σ-density – $a_1(C_{4v})$ symmetry (b), the Re–Re π-density – $e(C_{4v})$ symmetry (c), and Re–Re δ-density – b_2 (C_{4v}) symmetry (d); see Fig. 15 for symmetry notations and a correlation diagram within the C_{4v} subgroup, common for the dimer D_{4h} $Re_2Cl_8{}^{2-}$ and the $ReCl_4{}^-$ fragment

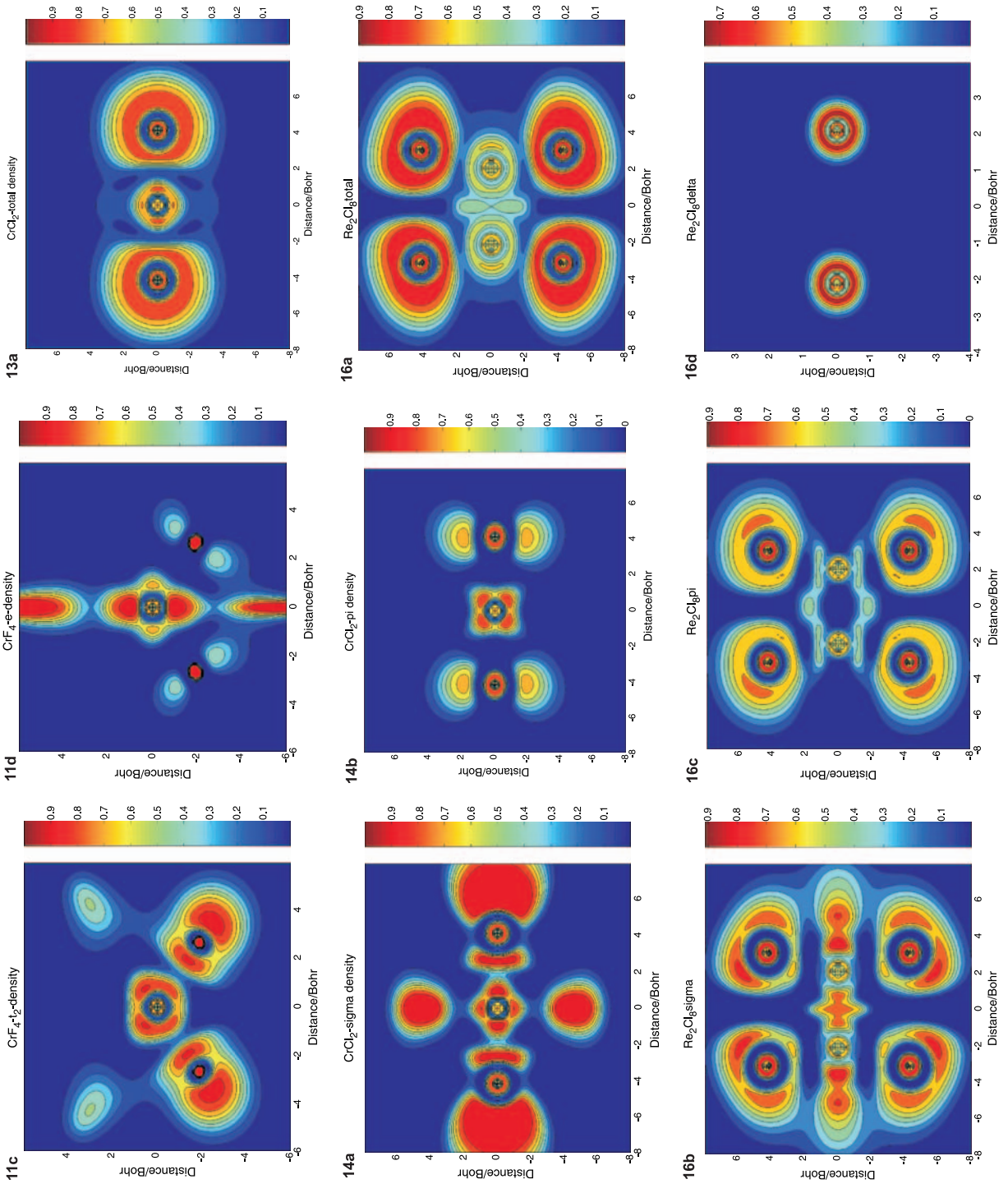
13a
CrCl2-total density
11d
CrF4-e-density
11c
CrF4-t2-density
16a
Re2Cl8total
14b
CrCl2-pi density
16c
Re2Cl8pi
16d
Re2Cl8delta
14a
CrCl2-sigma density
16b
Re2Cl8sigma
Distance/Bohr

Table 6. Energy partitioning analysis of tetrahedral Cr(IV) tetrahalides (X = F,Cl,Br,I) using atomic (Cr, F_4) or ionic (Cr^{4+}, $X_4{}^{4-}$) fragments (energy values in eV)[a], optimized Cr–X bond distances (R in Å)[b], *Mulliken* charges (q_{Cr}, q_X), and estimated values for ligand field splitting parameters 10Dq; percentages of E_{Elstat} and E_{orb} to total attractive energy $E_{Elstat} + E_{orb}$ as well as contributions from orbitals of different symmetry to ΔE_{orb} ($\Delta E_{orb} = \Delta E_{orb}(a_1) + \Delta E_{orb}(e) + \Delta E_{orb}(t_2) + \Delta E_{orb}(t_1)$) are given in parenthesis

	CrF_4		$CrCl_4$		$CrBr_4$		CrI_4	
R	1.741		2.141		2.311		2.540	
q_{Cr}	1.97		0.32		0.43		−0.70	
q_X	−0.49		−0.08		−0.11		0.18	
10Dq ≅ $e(4t_2) - e(2e)$	1.25		0.86		0.74		0.64	
Fragments	neutral[c] Cr, F_4	ionic[d] Cr^{4+}, $F_4{}^{4-}$	neutral[c] Cr, Cl_4	ionic[d] Cr^{4+}, $Cl_4{}^{4-}$	neutral[c] Cr, Br_4	ionic[d] Cr^{4+}, $Br_4{}^{4-}$	neutral[c] Cr, I_4	ionic[d] Cr^{4+}, $I_4{}^{4-}$
ΔE_{Prep}	–	115.06 [124.10]	–	111.15	–	109.45	–	108.31
ΔE_{int}	−29.17	−144.23 [−187.92]	−21.44	−132.59	−19.08	−128.53	−16.47	−124.78
ΔE_{Pauli}	33.06	19.52 [10.36]	23.99	15.99	19.98	13.01	15.53	10.93
ΔE_{Elstat}	−13.91 (22)	−113.38 (69) [−133.33]	−13.28 (29)	−89.97 (60)	−12.47 (32)	−78.63 (56)	−10.84 (34)	−72.32 (53)
ΔE_{orb}	−48.32 (78)	−50.37 (31) [−64.96]	−32.16 (71)	−58.61 (40)	−26.60 (68)	−62.91 (44)	−21.15 (66)	−63.38 (47)
$\Delta E_{orb}(a_1)$	−0.03 (0)	−2.34 (5) [−6.90]	−0.06 (0)	−3.00 (5)	−0.09 (0)	−3.46 (5)	−0.26 (1)	−3.54 (6)
$\Delta E_{orb}(e)$	−1.56 (3)	−32.53 (64) [−20.74]	−1.05 (3)	−35.96 (61)	−0.58 (2)	−37.23 (59)	−0.28 (1)	−36.50 (58)
$\Delta E_{orb}(t_2)$	−46.53 (96)	−13.41 (27) [−37.32]	−30.97 (96)	−16.99 (29)	−25.87 (97)	−19.36 (31)	−20.62 (97)	−21.33 (34)
$\Delta E_{orb}(t_1)$	−0.20 (0)	−2.08 [0.00] (4)	−0.07 (0)	−2.66 (4)	−0.05 (0)	−2.86 (4)	0.00 (0)	−2.03 (3)

[a] $M_s = 1$ spin-unrestricted, basis: TZP, non-relativistic, frozen cores: Cr up to 3p, X: up to 1s(F), 2p(Cl), 3d(Br), 4d(I), *PW*91 functional, calculation with single zeta (SZ) – basis for CrF_4 using ionic fragments is given in square brackets; [b] $M_s = 1$ spin-unrestricted, LDA functional; [c] $Cr(d^6)$, $F_4(a_1{}^2t_2{}^6a_1{}^2t_2{}^6e^4t_1{}^6t_2{}^2)$, spin-restricted reference fragments; [d] $Cr(d^2)$, $F_4{}^{4-}$ $(a_1{}^2t_2{}^6a_1{}^2t_2{}^6e^4t_1{}^6t_2{}^6)$, spin-restricted reference fragments

concerned. However, for the quantity ΔE_{orb} they allow to differentiate between covalency and polarization. Comparing $|\Delta E_{orb}(e)|$ with $|\Delta E_{orb}(t_2)|$ we get the correct relations $|\Delta E_{orb}(e)| < |\Delta E_{orb}(t_2)|$, as well as an exactly vanishing $|\Delta E_{orb}(t_1)|$ energy and most importantly, an increase of the $|\Delta E_{orb}(a_1)|$ energy. This is also the trend expected for orbitals which are occupied (e) and empty (a_1) on the Cr^{4+} fragments.

Finally, we should note that the value of the spectroscopic 10Dq parameter, given by the difference of energies between the antibonding orbitals $4t_2 - 2e$, does also follow the trend observed for the difference between the bonding energies $|\Delta E_{orb}(t_2)| - |\Delta E_{orb}(e)|$ (Table 6) – both quantities decrease from left to right along the CrF_4, $CrCl_4$, $CrBr_4$, CrI_4 series. This is similar to the results obtained for octahedral complexes.

III.3. CrX_2 Molecules ($X = F,Cl,Br,I$)

For linearly coordinated Cr(II) which is a d^4 ion, the AOM predicts a splitting of the d-orbitals into $\sigma_g(d_{z2})$ having the highest energy, followed by $\pi_g(d_{xz,yz})$ the two orbitals being placed by the AOM as $2e_\sigma$ and $2e_\pi$ above $\delta_g(d_{xy},d_{x2-y2})$. The latter orbital has no ligand counterparts and is thus purely non-bonding. In contradiction to this AOM prediction, the *KS*–MO diagram (Fig. 12) shows that the $3d_\sigma$ MO level is rather low lying because of the 3d–4s interaction, while $3d_\pi$ is found to be the topmost orbital: a consequence of the pronounced π-donor effect of the halide ligand. The metal–ligand bond-distances, decrease when lowering the coordination number (CN), as can be seen from a comparison with the four-fold and six-fold coordinated complexes with the same ligands. The extent of 3d–4s mixing increases from CrF_2 to CrI_2, *i.e.*, with increasing covalency, but the overall spread of MO energies decreases indicating a lowering of the bond strength along the same sequence. In spite of the higher degree of covalency for the CN=2 *versus* the CN=4 and CN=6 species, we find, both for ELF (for $CrCl_2$) and for the Laplacian of the electron density (for CrI_2), a mainly ionic bonding. In Fig. 13 we compare the two plots using the total density: no charge concentration between the Cr and *X* nuclei could be located. However, partitioning of the density into contributions due to σ and π bonding (Figs. 14a,

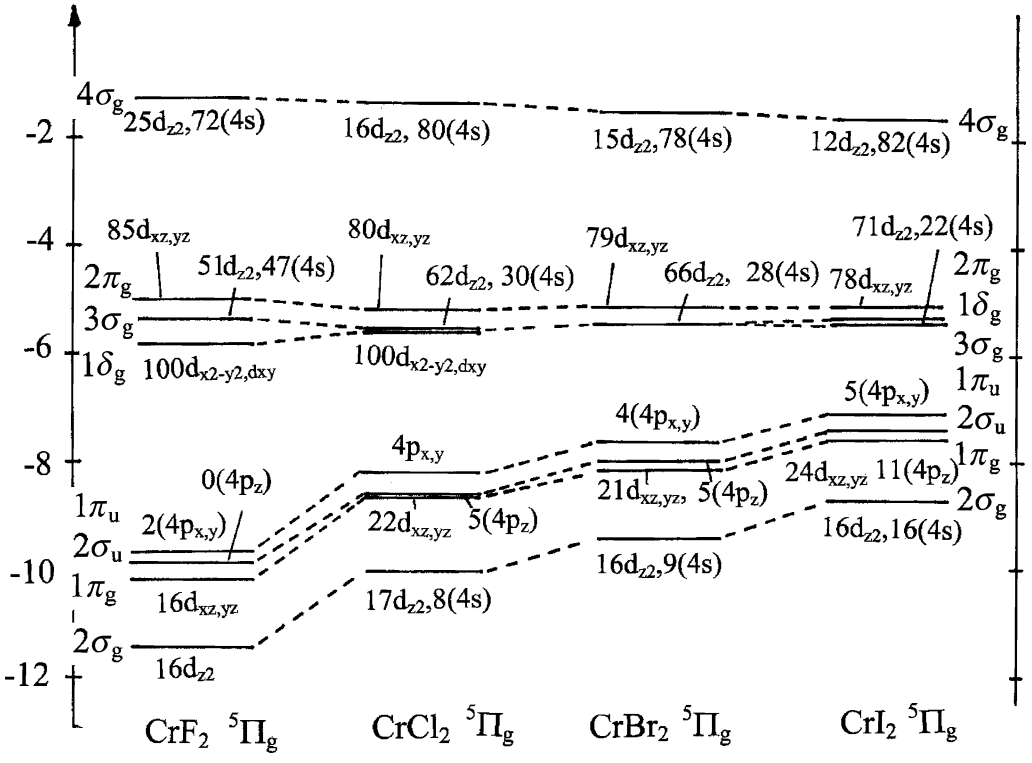

Fig. 12. *KS*-MO diagram for linear CrX_2 ($X = F,Cl,Br,I$) molecules in their equilibrium geometries and $^5\Pi_g$ ground state; percentages of contributions from Cr 3d, 4s, and 4p orbitals are included (without brackets for 3d, with "( )" brackets for 4s, and with "[ ]" brackets for 4p

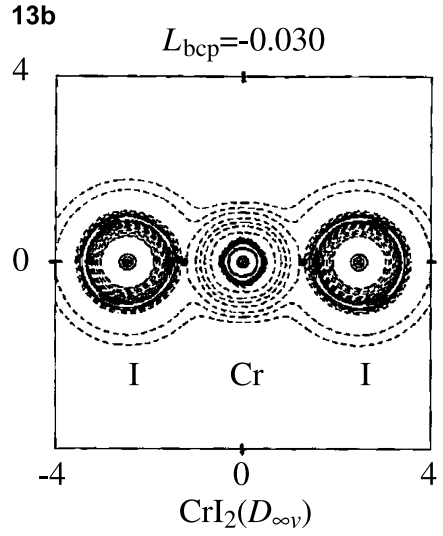

Fig. 13. Contour plots based on the total density for the electron localization function for $CrCl_2$ in (a) and Laplacian of the electron density for CrI_2 in (b); the value of the Laplacian at the bond critical point (L_{bcp}) for CrI_2 is given; the plots reflect overall ionic bonding

14b), impressively reflects a localization of valence domains. As one can immediately see, σ-bonding makes the main contribution, localization of spin-density due to π-bonding domains being much less pronounced. The latter can be easily understood in terms of the $^5\Pi_g$ ground state with four unpaired electrons. Three of them occupy the non-bonding $3\sigma_g$ and $1\delta_g$ orbitals and one is placed into the strongly antibonding $2\pi_g$ orbitals. Figure 14a nicely illustrates the effect of hybridization for strengthening of the metal–ligand bond as reflected by the in-phase h_1 hybrid, and the diminishing effect of the antibonding electron pair in the out-of-phase, h_2 hybrid (Eq. (14)), thus converting the latter into a nearly non-bonding lone-pair.

$$h_1 = \frac{1}{\sqrt{2}}(3dz^2 + 4s)$$
$$h_2 = \frac{1}{\sqrt{2}}(3dz^2 - 4s) \qquad (14)$$

The ETS energy decomposition analysis brings a further support to these results. In Table 7, we list the results from such analysis, where both, neutral and ionic reference fragments have been taken into account. The data clearly show that it is the ionic description which yields a picture that is consistent with respect to both the *KS*–MOs and ELF analysis. That is, the dominance of σ interaction as well as the nearly vanishing influence of π metal–ligand interactions. We notice the large negative value of $\Delta E_{orb}(\delta_g)$ emerging from an ionic description. This is found to be mostly an orbital polarization effect (*vide supra*). Thus, reducing the quality of the basis from TZP to SZ leads to a distinct lowering of this energy at the expense of accuracy of the description of the total bonding (SZ, CrF_2,

Table 7. Energy partitioning analysis of tetrahedral Cr(II) dihalides (X = F,Cl,Br,I) using atomic (Cr, F) or ionic (Cr^{2+}, X^-) fragments (energy values in eV)[a], optimized Cr–X bond distances (R in Å)[b], *Mulliken* charges (q_{Cr}, q_X), and estimated values for the ligand field splitting parameters $\Delta_1 = \sigma(d_{z2}) - \pi(d_{xz,yz})$, $\Delta_2 = \sigma(d_{z2}) - \delta(d_{x2-y2,xy})$; percentages of E_{Elstat} and E_{orb} to total attractive energy $\Delta E_{Elstat} + \Delta E_{orb}$ are given in parenthesis

	CrF_2		$CrCl_2$		$CrBr_2$		CrI_2	
R	1.806		2.208		2.375		2.609	
q_{Cr}	1.12		0.59		0.62		0.09	
q_X	−0.56		−0.29		−0.31		−0.05	
$\Delta_1 = \sigma(d_{z2}) - \pi(d_{xz,yz})$	−0.37		−0.34		−0.32		−0.32	
$\Delta_2 = \sigma(d_{z2}) - \delta(d_{x2-y2,xy})$	0.45		0.06		−0.01		−0.10	
Fragments	atomic	ionic	atomic	ionic	atomic	ionic	atomic	ionic
ΔE_{Prep}	–	15.02	–	15.27	–	15.56	–	15.93
ΔE_{int}	−16.98	−32.00	−13.52	−28.79	−12.43	−27.99	−11.09	−27.02
ΔE_{Pauli}	16.58	11.74	15.08	8.89	13.78	7.53	12.39	6.10
ΔE_{Elstat}	−6.28	−31.59	−6.91	−25.72	−6.89	−23.65	−6.58	−21.25
	(19)	(72)	(24)	(68)	(26)	(67)	(28)	(64)
ΔE_{orb}	−27.29	−12.15	−21.69	−11.96	−19.32	−11.87	−16.91	−11.87
	(81)	(28)	(76)	(32)	(74)	(33)	(72)	(36)
$\Delta E_{orb}(\sigma_g)$	−8.85	−6.25	−7.20	−5.80	−6.19	−5.61	−5.34	−5.60
$\Delta E_{orb}(\sigma_u)$	−3.82	−0.31	−3.18	−0.51	−3.00	−0.66	−2.78	−0.72
$\Delta E_{orb}(\pi_g)$	−5.66	−0.37	−3.73	0.30	−2.93	0.58	−2.06	0.74
$\Delta E_{orb}(\pi_u)$	−7.38	−0.54	−5.97	−0.75	−5.53	−0.81	−5.03	−0.71
$\Delta E_{orb}(\delta_g)$	−1.61	−4.68	−1.65	−5.21	−1.68	−5.38	−1.72	−5.57

[a] $M_s = 2$ spin-unrestricted, basis: TZP, non-relativistic, frozen cores: Cr up to 3p, X: up to 1s(F), 2p(Cl), 3d(Br), 4d(I), *PW*91 functional; [b] $M_s = 2$ spin-unrestricted, LDA functional

$\Delta E_{orb}(\delta_g) = -1.60$ eV). An extensive DFT study of the structure and bonding in transition metal dihalides has been published by *Wang* and *Schwarz* and the reader is referred to this work for more details [41]. The comparison of calculated bond lengths, vibrational frequencies, and dissociation energies with experiment in Ref. [41] demonstrates the ability of the DFT method to correctly describe the electronic structure and bonding of these complexes. Our calculations are widely in agreement with all these studies. A mostly ionic bonding in TM dihalides MX_2 (M = Ca to Zn; X = F,Cl,Br) has also been reported based on a topological analysis of ELF. Likewise, bifurcation diagrams reported from a study of VO_x^+ and VO_x (x = 1–4) clusters [23] invariably show a mostly ionic V–O bonding in all these species (oxidation states of V – 5(d^0) and 4(d^1)). Thus the tree diagram of ELF for VO_2^+ with a bend geometry in its $^1A_1$ ground state shows core/valence bifurcations into oxygen core domain and a composite valence domain at ELF = 0.20. At a threshold value of ELF = 0.40, the composite valence domain is further split into a vanadium core domain and two mono synaptic oxygen domains, the latter two reflecting oxygen lone pairs. Very interestingly, the bifurcation diagram of VO_2 with a similar bend geometry shows a vanadium valence domain. Being monosynaptic, the latter reflects the single d-electron in the d-subshell of V. Without exceptions, no bi-synaptic (V–O) valence domains could be found in all these

examples, demonstrating once more the rather high ionicity of the V–O bond, which is found to be also independent on the coordination number.

III.4. Metal–Ligand and Metal–Metal Bonding in $Re_2Cl_8^{2-}$

The discovery of a strong Re–Re bond in the $Re_2Cl_8^{2-}$ anion in 1965 [42], termed quadruple bond, did open a new area in inorganic chemistry. Moreover, it contributed to initiate studies which helped, to understand and to validate our knowledge about the chemical bond, based on the classical paper by *Heitler-London* [43] and on the *Coulson-Fischer* treatment of the two-electron bond in the H_2 molecule [44]. An excellent review of all developments covering both experiment and theory on the δ bond in the Re_2^{6+} and Mo_2^{4+} cores along with reference to original work has been published recently [45].

To analyze the Re–Re bond in $Re_2Cl_8^{2-}$ it is reasonable to start from the two square pyramidal $ReCl_4^{2-}$ fragments. For this coordination, the $|5d\rangle$ orbitals of Re are split into $6a_1(d_{z2})$, $2b_2(d_{xy})$, $6e(d_{xz,yz})$, and $4b_1(d_{x2\text{-}y2})$ species whose energies and compositions are depicted in Fig. 15 (left). A qualitative understanding of this splitting pattern is illustrated using AOM expressions (Fig. 3). The d_{z2} orbital is antibonding, but is largely stabilized by the 5d–6s mixing which pushes it down, thus making it lowest in energy. This mixing is such, that it increases the lobes into the axial direction and thus enhances the Re–Re overlap in the dimer. It follows that the Re–Cl bonding in the $ReCl_4^-$ fragment, which leads to 5d–6s hybridization has an *indirect enforcing effect* on the Re–Re σ-bond. Thus, considerations of a naked Re_2^{6+} cluster leads to a much weaker splitting of the σ-orbitals (Fig. 15 right hand side). The energies of the 6e and $2b_2$ orbitals of the $ReCl_4^-$ unit indicate a strong Re–Cl π-bonding interaction (out-of-plane and in-plane, for 6e and $2b_2$, respectively) and are calculated at almost the same energy. They give rise to Re–Re π and δ bonds, respectively. All four orbitals, $6a_1$, $2b_2$, and 6e are singly occupied in $ReCl_4^-$ and give rise to four bonds between the two $ReCl_4^-$ – units: one σ, two π, and one δ bond. A rough measure for the strength of these bonds is the spitting of the $a_1(9a_1, 12a_1)$, e(11e, 12e), and $b_2(3b_2, 4b_2)$ orbitals, which are calculated to be 5.42, 3.58, 0.70 (Fig. 15), respectively, thus reflecting a decrease of bond strength from σ to π to δ. This is clearly manifested by the ELF plots for these pathways as is nicely seen in Fig. 16. Thus, while the plot in Fig. 16a does not show any indication of accumulation of electron charge between the Re nuclei, the symmetry partitioned ELF plots (Figs. 16b, 16c) nicely reflect this. The spectacular feature of these plots is the σ-bond pathway which shows a valence domain between the Re nuclei but not only. Indeed, the plot for π symmetry reflects a much weaker yet non-negligible bonding effect, while the one for δ does not display any bonding features. Apparently, the δ-bonding in $Re_2Cl_8^{2-}$ can be regarded as a weak bond which might rather be considered as a strong antiferromagnetic coupling between the unpaired spins of δ-symmetry (see below). This interaction can be fully destroyed when going from the eclipsed (D_{4h}) to the staggered (D_{4d}) conformation as is shown by the *KS*–MO diagram (Fig. 17). For this geometry, the δ-orbitals are rotated by a 45° with respect to each other, leading to strict orthogonality and to ferromagnetism. This could be achieved by chemical manipulations [45]. The ETS energy decomposition analysis lends support to this interpretation

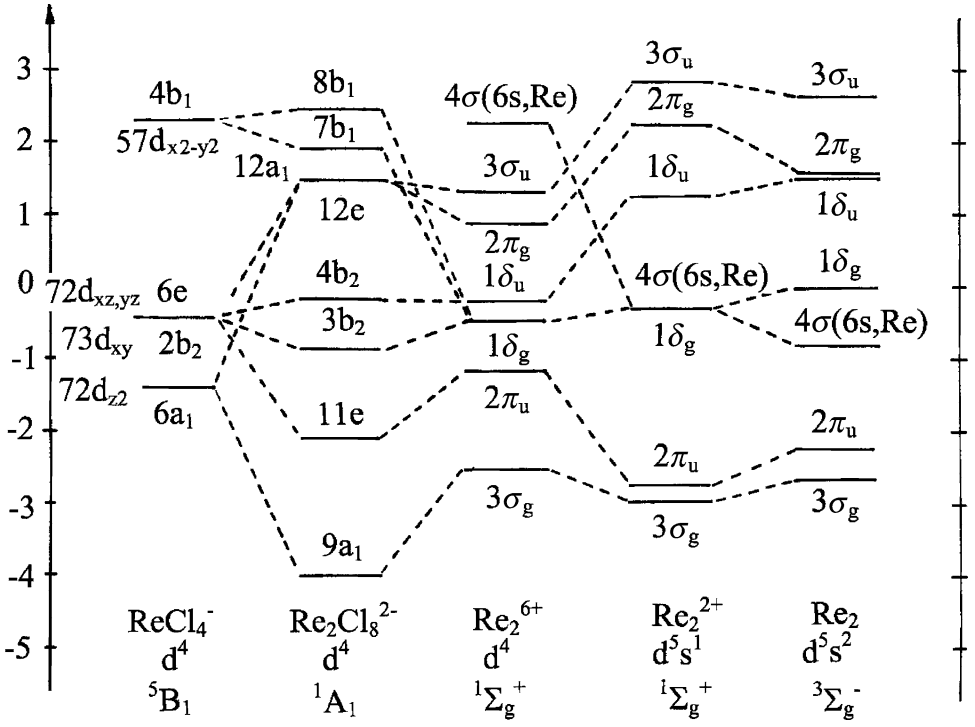

Fig. 15. *Kohn-Sham* MO energy diagram for $Re_2Cl_8^{2-}$ and its correlation with the *KS*-MO levels dominated by 5d orbitals and their percentages of the constituting $ReCl_4^-$ (C_{4v} symmetry) fragment; *KS*-MO energy diagrams for the Re_2^{6+}, Re_2^{2+}, and Re_2 dimers are included; for the sake of a better comparison, *KS*-MO energies for each cluster have been plotted taking their baricenter energy as a reference; electronic ground state notations refer to C_{4v} (common symmetry for $ReCl_4^-$ and $Re_2Cl_8^{2-}$) and $D_{\infty h}$ (for Re_2^{6+}, Re_2^{2+}, Re_2); the shift of the *KS*-MO with dominating contribution of 6s toward lower energies from Re_2^{6+}, Re_2^{2+}, and Re_2 is indicated; the high energy position of this orbital for $Re_2Cl_8^{2-}$ and $ReCl_4^-$ is found to be outside the plotted energy range and is not shown; electronic configurations of the Re fragments and the electronic states used for the DFT calculations on the dimers are given at bottom

based on MO analysis and ELF plots (Table 8). The absence of δ-bonds in the D_{4d} geometry also explains the larger stability (by -0.65 eV for ΔE_{int}) of the eclipsed compared to the staggered form. The ΔE_{int} energy change when going from the D_{4h} to the D_{4d} complex is a result of the balance between the ΔE_{Pauli} term (which is in favor for the D_{4d} geometry, $\delta\Delta E_{Pauli} = -0.59$ eV) and ΔE_{orb} ($\delta\Delta E_{\text{orb}} = 1.02$), and to a lesser extend to the ΔE_{Elstat} term ($\delta\Delta E_{\text{Elstat}} = 0.23$ eV, *i.e.*, both are in favor of the D_{4h} geometry). It is interesting to note that all contributions to ΔE_{orb} become less negative when going from D_{4h} to D_{4d}. However, reduction in bond strength in this direction is dominated by δ [$\delta\Delta E_{\text{orb}}(\delta) = 0.73$ eV], followed by π and then by σ [$\delta\Delta E_{\text{orb}}(\pi) = 0.19$ and $\delta\Delta E_{\text{orb}}(\sigma) = 0.11$ eV].

The metal–metal interactions in complexes M_2(formamidinate)$_4$ including various metals (M = Nb, Mo, Tc, Ru, Rh, and Pd) with different d-electron counts and M–M bond orders have been studied in terms of the topological analysis of the electron density and ELF by *Silvi et al.* [46]. The AIM analysis of the calculated

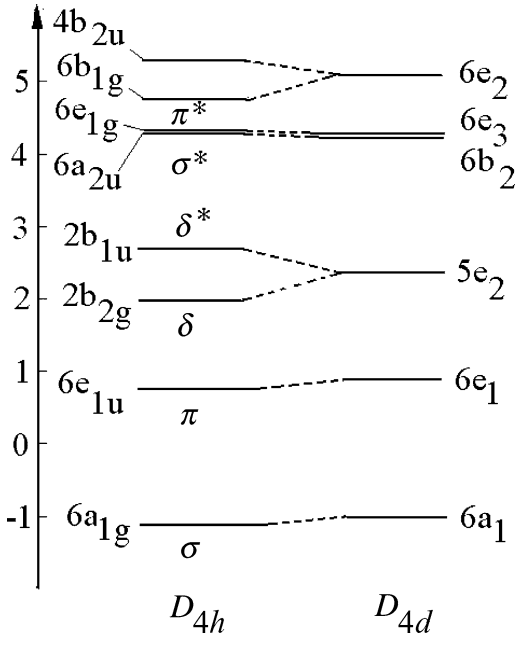

Fig. 17. Energies of metal centered 5d *KS*-MOs for $Re_2Cl_8^{2-}$ in its more stable, eclipsed (D_{4h}), and in its less stable, staggered (D_{4d}) conformations and the correlation between them; the suppression of the Re–Re δ-bond when going from the D_{4h} to the D_{4d} geometry and the assignment of the MOs to σ, π and δ bonding (σ, π, and δ) and antibonding (σ^*, π^*, and δ^*) are shown

Table 8. The unique bonding situation in $Re_2Cl_8^{2-}$ with a bonding energy partitioned with respect to two non-interacting $ReCl_4^{1-}$ sub-units in its eclipsed (ideal for δ-bonding) and its staggered (δ-bonding is abolished) conformations[a]

ΔE_{Pauli}	$\Delta E_{\mathrm{Elstat}}$	ΔE_{orb}	ΔE_{int}	$\Delta E_{\mathrm{orb}}(a_1)$	$\Delta E_{\mathrm{orb}}(a_2)$	$\Delta E_{\mathrm{orb}}(b_1)$	$\Delta E_{\mathrm{orb}}(b_2)$	$\Delta E_{\mathrm{orb}}(e)$
eclipsed[b]								
25.46	−10.31	−20.79	−5.64	−10.63	0.00	−0.07	−0.80	−9.29
staggered[c]								
24.87	−10.08	−19.77	−4.99	−10.52	0.00	−0.08	−0.08	−9.10

[a] Scalar relativistic ZORA calculations; [b] $a_1^2(\sigma)e(\pi)^4b_2(\delta)^2$ – singlet ground state; [c] $a_1^2(\sigma)e(\pi)^4b_2(\delta)b_1(\delta)$ – triplet ground state, C_{4v} symmetry notations

electron density show low $\rho(\mathbf{r})$ values at the metal–metal bond critical points and therefore turn out to be not very informative. Using ELF instead, four bisynaptic metal–metal valence basins, *V*(*M*–*M*) could be located for the Mo and Nb dimers, reflecting a bonding situation, similar to that for $Re_2Cl_8^{2-}$. Only one metal–metal valence basin has been found for the Ru and Rh complexes, while no disynaptic basins are obtained for the Tc and Pd systems. In all cases, the *V*(*M*–*M*) valence basins are not the dominant features of the interactions due to their low population values with main contributions from the metal ''4d'' electrons, as expected. However, the ''4d'' electrons have been found to contribute mostly to the metal core basins. As the most important feature of the metal–metal bond in these systems it

was noted the very high metal–metal core and the AIM atomic covariancies – $B(M, M)$ and $\lambda_c(\rho)$, respectively. Both reflect a rather large electronic charge fluctuation between the two metallic cores. These have been interpreted in terms of simple resonance arguments [46]. Except for the Rh compound, a nice correlation between $B(M, M)$ and the metal–metal distances has been found.

Yet, another possibility to analyze Re–Re σ, π, and δ bonds within DFT is to apply to each of them separately the two-center-two-electron bond model. For σ and δ this can easily be done, because for each type of bonding, there are two MOs and two available electrons in D_{4h} symmetry. This is similar to a discussion of bonding in these systems in which δ-electrons are being considered as decoupled from the π- and the σ-electrons (*Bursten* and *Clayton* [47]). Within this approximation, an analysis along the lines of a homonuclear diatomic MO problem for each of the two bonding modes separately becomes possible. For π-bonds, there are 4 electrons and 4 orbitals which makes the analysis cumbersome. However, also in this case, an approximate treatment can be given, restricting the consideration to two electrons distributed over *only* two orbitals – bonding and antibonding, each of them transforming as *one* of the components of the doubly degenerate orbital e.

We present here a new bond analysis using the following procedure. Let us assume that two semi-occupied orbitals dl_1 and dl_2 located on both symmetry equivalent fragments couple to yield an in-phase (a) and an out-of-phase (b) MO (Eq. (15)) where a and b belong to two different irreps.

$$\begin{aligned} a &= \frac{1}{\sqrt{2}}(dl_1 + dl_2) \\ b &= \frac{1}{\sqrt{2}}(dl_1 - dl_2) \end{aligned} \tag{15}$$

Moreover we neglect here the overlap between dl_1 and dl_2. Six micro-states or Single Determinants (SD) are possible. Two are doubly occupied $|a^+a^-|$, $|b^+b^-|$ and four are singly occupied $|a^+b^-|$, $|a^+b^+|$, $|a^-b^+|$, $|a^-b^-|$. The doubly occupied SD have $a \otimes a = b \otimes b = A$ spatial symmetry, correspond to closed shells, and are spin singlets. The SD based on singly occupied spinorbitals have $a \otimes b = B$ spacial symmetry and correspond to a singlet and to a triplet. The two SD with $M_S = 0$: $|a^+b^-|$ and $|a^-b^+|$, belong both to a singlet and to a triplet. The energies of all these determinants can be calculated from DFT. Let us denote their energies by Eq. (16).

$$\begin{aligned} &E_1 = E(|a^+a^-|), \quad E_2 = E(|b^+b^-|), \quad E_3 = E(|a^+b^+|) = E(|a^-b^-|), \\ &E_4 = E(|a^+b^-|) = E(|a^-b^+|) \end{aligned} \tag{16}$$

We note that the difference $E_4 - E_3$ equals the exchange integral [ab|ab] which is also the quantity accounting for the mixing (1:1 in the limit of a full localization) between the $|a^+a^-|$ and $|b^+b^-|$ microstates. This leads to the secular Eq. (17) which after diagonalization yields the eigenvalues E_- and E_+ and the energy separation between the lowest singlet state and the triplet $E_- - E_3$, referred to as the singlet-triplet splitting. The latter is identical to the exchange integral in magnetism. It is a good measure for the covalence stabilization of a bonding

electron pair with respect to a non-bonding triplet pair. When compared in the limit of complete dissociation these quantities yield the total bonding energy (Eq. (17)).

$$\begin{bmatrix} E_1 & (E_4 - E_3) \\ (E_4 - E_3) & E_2 \end{bmatrix} \tag{17}$$

Let us now consider the formation of bonding in terms of a localized model for bonding. Within such a model (*Anderson* [48]), dl_1 and dl_2 are singly occupied in the ground state for separate fragments giving rise to a triplet and to a singlet with wavefunctions ψ_T and ψ_S (Eqs. (18) and (19)). There are two further singlet states ψ_S^{CT} and $\psi_S'^{CT}$ arising when either of the two magnetic electrons is transferred to the other magnetic orbital (SOMO) (Eqs. (18) and (19)). ψ_S lies by $2K_{12}$ at higher energy than ψ_T.

$$\psi_T = \left|\, dl_1^+\, dl_2^+ \right|, \quad \left|\, dl_1^-\, dl_2^- \right|, \quad \frac{1}{\sqrt{2}}\left(\left|\, dl_1^+\, dl_2^- \right| + \left|\, dl_1^-\, dl_2^+ \right|\right) \tag{18}$$

$$\psi_S = \frac{1}{\sqrt{2}}\left(\left|\, dl_1^+\, dl_2^- \right| - \left|\, dl_1^-\, dl_2^+ \right|\right), \quad \psi_S^{CT} = \frac{1}{\sqrt{2}}\left(\left|\, dl_1^+\, dl_1^- \right| + \left|\, dl_2^+\, dl_2^- \right|\right),$$
$$\psi_S'^{CT} = \frac{1}{\sqrt{2}}\left(\left|\, dl_1^+\, dl_1^- \right| - \left|\, dl_2^+\, dl_2^- \right|\right) \tag{19}$$

We take the energy of the latter state as reference $\{E(\psi_T) = 0\}$. K_{12} is the classical *Heisenberg* exchange integral (Eq. (20)) which is always positive.

$$K_{12} = \iint dl_1(1)^* dl_2(1) \frac{1}{r_{12}} dl_1(2)^* dl_2(2) dV_1 dV_2 = [dl_1 dl_2 | dl_1 dl_2] \tag{20}$$

It reflects the exchange stabilization of the triplet over the singlet due to gain in potential energy connected with the spatial extension of the *Fermi* (exchange) hole (potential exchange). The ψ_S two-electron wave-function can mix with the charge transfer state $\psi_S{}^{CT}$. Its energy, denoted with U equals the difference between the *Coulomb* repulsions of two electrons on the same center, *i.e.*: $\left|\, dl_1^+\, dl_1^- \right|$ or $\left|\, dl_2^+\, dl_2^- \right|$ ($U_{11} = [dl_1 dl_1 | dl_1 dl_1] = U_{22} = [dl_2 dl_2 | dl_2 dl_2]$) and when they are located on different centers (the notation $U_{12} = [dl_1 dl_1 | dl_2 dl_2]$ applies). The energy separation between the $dl_1{}^2$ (or $dl_2{}^2$) excited state and the $dl_1{}^1 dl_2{}^1$ ground state configuration is given by Eq. (21).

$$U = U_{11} - U_{12} \tag{21}$$

U is also a positive quantity. The interaction matrix element between ψ_S and $\psi_S{}^{CT}$ (Eq. (22)) reflects the delocalization of the bonding electrons due to orbital overlap. The quantity $t_{12} = \langle dl_1 | h | dl_2 \rangle$ is being referred to as the transfer (hopping) integral between the two sites.

$$\langle \psi_S | H | \psi_S^{CT} \rangle = 2T_{12} = 2(t_{12} + [dl_1 dl_1 | dl_1 dl_2]) \tag{22}$$

Calculations show that $T_{12} = t_{12}$ in a very good approximation, differences being generally less than 0.002 eV. This term tends to lower the singlet-over the triplet-energy and is intrinsically connected with the gain of kinetic energy (kinetic

exchange). The interaction matrix (Eq. (23)) describes the combined effect of these two opposite interactions.

$$\begin{matrix} & \psi_{\mathrm{S}} & \psi_{\mathrm{S}}^{\mathrm{CT}} \\ \begin{matrix} \\ \\ \end{matrix} & \begin{bmatrix} 2K_{12} & 2T_{12} \\ 2T_{12} & U + 2K_{12} \end{bmatrix} \end{matrix} \tag{23}$$

As has been pointed out already in Ref. [49], the parameters K_{12}, U, and T_{12} can be expressed in terms of the *Coulomb* integrals (J_{aa}, J_{bb}, and J_{ab}), the exchange integral K_{ab}, and of $\varepsilon(\mathrm{b}) - \varepsilon(\mathrm{a})$, the *KS*-orbital energy difference. Eqs. (24)–(26) below, resume these relations.

$$K_{12} = \frac{1}{4}(J_{\mathrm{aa}} + J_{\mathrm{bb}} - 2J_{\mathrm{ab}}) = \frac{1}{4}(E_1 + E_2 - 2E_4) \tag{24}$$

$$U = U_{11} - U_{12} = 2K_{\mathrm{ab}} = 2(E_4 - E_3) \tag{25}$$

$$T_{12} \cong \frac{1}{2}\{\varepsilon(a) - \varepsilon(b)\} = \frac{1}{4}(E_2 - E_1) \tag{26}$$

We like to point out that these expressions are furthermore related with the energies of the single determinants $|\mathrm{a}^{+}\mathrm{a}^{-}|$, $|\mathrm{b}^{+}\mathrm{b}^{-}|$, $|\mathrm{a}^{+}\mathrm{b}^{+}|$, $|\mathrm{a}^{+}\mathrm{b}^{-}|$ (*i.e.*, E_1, E_2, E_3, and E_4, respectively). In deriving these expressions we implicitly made use of Eqs. (27)–(30).

$$E_1 = 2\varepsilon(\mathrm{a}) + J_{\mathrm{aa}} \tag{27}$$

$$E_2 = 2\varepsilon(\mathrm{b}) + J_{\mathrm{bb}} \tag{28}$$

$$E_3 = \varepsilon(\mathrm{a}) + \varepsilon(\mathrm{b}) + J_{\mathrm{ab}} - K_{\mathrm{ab}} \tag{29}$$

$$E_4 = \varepsilon(\mathrm{a}) + \varepsilon(\mathrm{b}) + J_{\mathrm{ab}} \tag{30}$$

Thus, Eqs. (24)–(26) allow us to obtain K_{12}, U, and T_{12} directly from DFT enabling an analysis of the chemical bond. We get therefore a bonding model in terms of localized orbitals, whose parameters are readily obtained from the DFT SD energies E_1, E_2, E_3, and E_4 of the *dinuclear complex*. It is remarkable that the same model can be applied with success to magnetic exchange coupling [50], thus, making it possible to consider magnetic and bonding phenomena on the same footing. In fact, there is no fundamental difference between antiferromagnetism and bonding.

In Table 9 we list the energies of E_1, E_2, E_3, E_4, the corresponding eigenvalues E_{-}, E_{+}, E_{T}, E_{S}, and the singlet triplet separation J_{12} obtained from DFT calculations. Re–Re bond energies decrease from σ to π to δ following the lines of the MO and the ETS analysis. It is interesting to note that the $\delta\varepsilon(\lambda)$ ($\lambda = \sigma, \pi, \delta$) splittings of the *KS*–MO energies and $J_{12}(\lambda)$ are very close in magnitude and nearly equal to the values of the hopping integral t_{12}. This reflects the common covalent origin of these parameters. At the same time, $\Delta E_{\mathrm{orb}}(\lambda)$ deduced from the ETS analysis are larger than $J_{12}(\lambda)$ and $\delta\varepsilon(\lambda)$ (Table 9). Possibly, polarization effects contribute to this difference (see above). The parameter K_{12} is just the ferromagnetic exchange integral which may become operational in the limit of zero overlap. It leads to a

Table 9. Singlet *versus* triplet ground state stabilizations in eclipsed $Re_2Cl_8^{2-}$ based on a two-electron-two-center bond model within the single determinant DFT approach for σ, π, and δ bonds[a]

$\lambda =$	σ	π	δ
$E_1(a^+a^-)$	−51.543 (−49.278)	−51.543 (−49.278)	−51.543 (−49.278)
$E_2(b^+b^-)$	−40.115 (−38.893)	−44.029 (−42.467)	−50.105 (−47.966)
$E_3(a^+b^+)$	−46.287 (−44.513)	−48.076 (−46.156)	−51.148 (−48.919)
$E_4(a^+b^-)$	−46.091 (−44.285)	−47.906 (−46.008)	−50.833 (−48.631)
$E_-\ ^1(\lambda\lambda)$	−51.546 (−49.283)	−51.546 (−49.281)	−51.609 (−49.338)
$E_+\ ^1(\lambda^*\lambda^*)$	−40.112 (−38.888)	−44.025 (−42.464)	−50.039 (−47.906)
$E_T\ ^3(\lambda\lambda^*)$	−46.287 (−44.513)	−48.076 (−46.156)	−51.148 (−48.919)
$E_S\ ^1(\lambda\lambda^*)$	−45.896 (−44.057)	−47.736 (−45.860)	−50.518 (−48.343)
$J_{12} = E_- - E_T$	−5.259 (−4.769)	−3.470 (−3.125)	−0.461 (−0.419)
$\delta\varepsilon(\lambda)$	−5.41	−3.58	−0.704
$\Delta E_{orb}(\lambda)$	−10.633	−9.287	−0.802
K_{12}	0.131 (0.100)	0.060 (0.068)	0.004_5 (0.004_5)
t_{12}	5.714 (5.192)	3.757 (3.406)	0.719 (0.656)
U	0.391 (0.456)	0.340 (0.296)	0.630 (0.576)

[a] Scalar relativistic (non-relativistic, in parenthesis) spin-unrestricted ZORA calculations in D_{4h} symmetry with the following configurations for the Re d-orbitals (see Fig. 17) for σ, π and δ bonding: $(a^+a^-) = 6\underline{a}_{1g}{}^2 6e_{1u}{}^4 2\underline{b}_{2g}{}^2$; $(b^+b^-) = 6\underline{a}_{2u}{}^2 6e_{1u}{}^4 2b_{2g}{}^2$, $6a_{1g}{}^2 6e_{1u}{}^2 6\underline{e}_g{}^2 b_{2g}{}^2$, $6a_{1g}{}^2 6e_{1u}{}^4 2\underline{b}_{1u}{}^2$; ($a^+b^+$ and a^+b^-) $= 6\underline{a}_{1g}{}^1 6a_{2u}{}^1 6e_{1u}{}^4 2b_{2g}{}^2$; $6a_{1g}{}^2 6\underline{e}_{1u}{}^3 6\underline{e}_g{}^1 2b_{2g}^2$; $6a_{1g}{}^2 6e_{1u}{}^4 2\underline{b}_{2g}{}^1 2\underline{b}_{1u}{}^1$ (a, b orbitals under consideration are underlined); values of the transfer (hopping) integral t_{12}, the *Heisenberg* exchange integral (K_{12}), and the effective transfer energy (U) are also included; Re–Re (2.236 Å) and Re–Cl (2.331 Å) bond distances are obtained from LDA-DFT geometry optimizations

triplet ($^3A_2$) ground state in the staggered (D_{4d}) conformation of $Re_2Cl_8^{2-}$ where δ bonding is fully suppressed.

IV. Discussion and Conclusions

A chemist considers a molecule as a system of atoms and bonds, a quantum chemist treats it as a system of interacting electrons and nuclei. A possible bridge between these two approaches is the LCAO method which is a useful tool for calculation and interpretation. However, a rigorous quantum theory of atomic interactions is still lacking. *Mayer*'s ''Chemical'' Hamiltonian [51–53] offers a deductive approach which allows *a priori* of making an analysis rather than *a posteriori* (after having calculated the wavefunction). However, an application of this approach to open shell systems is still lacking. In this study, we applied the ETS method to TM complexes with open d-shells and compared results from analysis of the electron density using the Laplacian of the electron density and the electron localization function. From this comparison we can conclude, that starting from ionic bonding and introducing a correction for covalency (charge transfer) and polarization yields a consistent description, thus allowing to regard the TM–ligand bond as a donor–acceptor relationship. The classical coordination bond is relatively ionic and therefore electronic properties are focused mostly on the d^n-configuration of the TM. Such a concept is highly supported by the spectroscopic

behavior, which shows d–d transitions and CT-transition far apart, allowing to define what is called to be a typical *Werner* type complex. Electronic absorption and emission spectra and ESR and their interpretations using ligand field theory have been used to characterize electronically such compounds. These studies repeatedly demonstrate that ionic like d^n-configurations and the many electron states originating for them are well defined. In this sense this class of compounds differs from organometallic ones, where bonding is more covalent and electronic effects extend beyond the d^n manifold to include metal s and p valence orbitals as well.

The rather ionic character of the TM–ligand bond and the much smaller radius of the 3d compared to the 4s orbital has led to suggest that the TM–ligand bond is mainly governed by 4s and 4p-orbitals, whereas the 3d-electrons are inactive being mainly spectators (or spectroscopic probes) for the chemical bond [54]. Based on our analysis we cannot confirm this point. We find, that in *Werner* type complexes, the 3d electrons play a dominant role in bonding.

The bonding concept emerging from our analysis is illustrated in Fig. 18 taking CrF_4 as an example. Starting from neutral atoms, a large amount of preparation energy ΔE_{prep} is needed to produce ionic fragments, in this case we consider Cr^{4+}

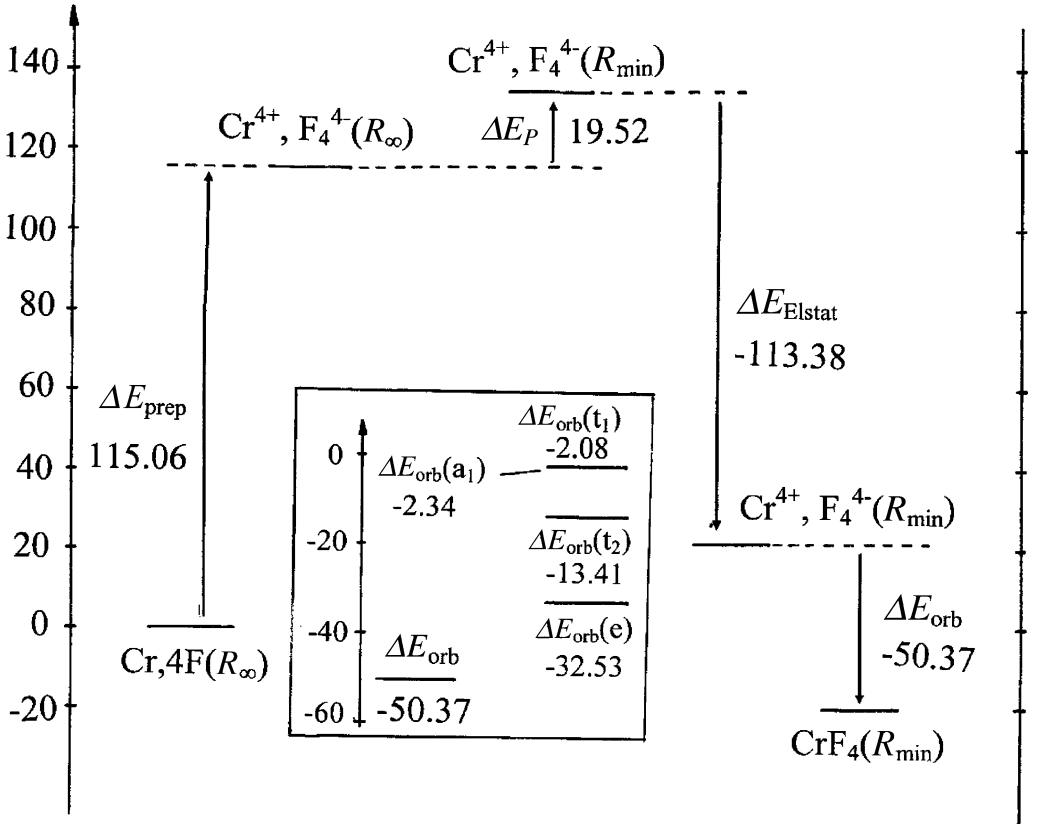

Fig. 18. The concept of ligand-to-metal donor–acceptor bonding energy for *Werner*-type complexes of transition metals with open d-shells and its components within the ETS energy decomposition scheme, illustrated for CrF_4

and F_4^{4-} at infinite distances. Bringing these moieties from infinity to their actual positions in the complex needs some additional energy due to *Pauli* (exchange) repulsion between closed shells denoted as, ΔE_P. The sum of these two terms defines the repulsive contribution to the bonding energy. The latter becomes largely overcompensated by the attractive part of the bonding energy. It consists of two components. The largest term, ΔE_{Elstat}, is the electrostatic (*Coulomb*) attraction between ions of oppositely charged ions. This is the molecular analogue of the *Madelung* energy in ionic crystals. Another stabilizing term, which is also chemically the most interesting one, is the orbital relaxation energy, ΔE_{orb}. It consists of electron charge-transfer between ions and additionally, of orbital polarization of the ions due to the electrostatic field of the neighboring orbitals. The ΔE_{orb} energy can be further decomposed into symmetry species. Their variation within classes of closely related molecules is chemically significant and bears power of interpretation.

The rather ionic nature of the TM–ligand bond in *Werner* type complexes also derives from analysis based on natural bond orbitals and their extensions, *i.e.*, the localized bond concept [55]. When combined with valence bond theory, this approach allows to locate most probable *Lewis* structures. Thus, sd^{n-1} hybride orbitals for a ML_n complex along with natural hybrid orbitals on the ligands yield a rather accurate approximation of valence electron density in many cases (up to 97–99% accuracy [55]). They show that the relative participation of $|4s\rangle$ TM orbitals to the TM–ligand bond increases with decreasing coordination number. This trend is very similar to, what we obtain presently: the inclusion of $|4s\rangle$ yields stronger bonds, when going, say from $CrCl_6^{3-}$ to $CrCl_4$ to $CrCl_2$. Moreover, ionic resonance structures (such as $WF_3^{3+}(F^-)_3$, W=F double bonds, and presumably $ClCl_3(Cl^-)_3$, Cr–Cl single bonds) yield a high or dominating weight in the total wavefunction. Also, the existence and geometries, say of CrX_4 (X = F,Cl,Br,I) are in agreement with electron counts (4 sd^3 hybride functions plus 2 unpaired electrons = 6). The NBO approach is beyond the scope of the present review, see Refs. [56–58].

The ETS method has been found to be a useful tool in analyzing the TM-bond. However, results and interpretations are biased by the choice of reference fragments which might differ from case to case. Thus, other methods, based on analysis of the electron density of the considered molecule can provide information for the bonding ''as it is''. Thus, the quantum theory of atoms and molecules and the electronic localization function are valuable extensions and can assist interpretations by the ETS method. We have found that the former two approaches gain insight power for complexes of high symmetry when decomposition of the electron density into different irreducible representations of the molecular point group is possible. Using such symmetry resolved Laplacians and ELF functions enabled us to show that ionic bonding in *Werner* type TM complexes is considerably modified by covalency, mostly of σ-type, but turns out to be mainly ionic when looking at the total electron density.

A more critical remark should be made when considering the quantitative aspects of *Morokuma* and the closely related ETS methods. The former has been severely criticized from the Natural Bond Order perspective [59] as well as on grounds of basis-set related numerical instabilities [60]. It was suggested that the

Natural Energy Decomposition Analysis (NEDA) [61] emerges as a clear alternative being conceptually better justified and better converging to asymptotic classical entities. The main critique was directed to the decomposition using non-orthogonal fragments in the short-range region of covalent bonding, where, because of the larger overlap, conceptual ambiguities increase. It leads in the case of ETS to inaccuracies when calculating the ΔE_{Elstat} term, which further propagates into the ΔE_P and the ΔE_{orb} terms.

In this work, we applied the ETS model using two different starting approximations for the reference fragments – atomic and ionic ones. We have stated that it is the ionic reference point which provides a starting point for the rather localized d-electrons (and our analysis applies only to those cases). For localized d-electrons the ligand–metal overlap is very small and we think that the main arguments (the bigger overlap) against the ETS method does not hold for this class of compounds. In spite of this, we feel that other energy partitioning schemes, such as the NEDA deserve increased attention in the future. However, to our knowledge, the method has not yet been applied to TM compounds. We hope that the present study will stimulate some work in this direction.

Acknowledgements

The authors owe thanks to Prof. Dr. *G. Frenking* (Fachbereich Chemie, Philipps-Universität, Marburg, Germany) and the members of his group, and Prof. Dr. *C.-W. Schläpfer* (Fribourg) for a long standing discussion on the problems of the chemical bond and many helpful suggestions concerning this study. This work has been supported by the Bundesamt für Forschung and Wissenschaft (Swisse) and a COST action (D26-0013-02) within the European Science Foundation.

References

[1] Coppens P (1977) Angew Chem Int Ed Engl **16**: 32
[2] Morokuma K (1977) Acc Chem Res **10**: 294
[3] a) Ziegler T, Rauk A (1977) Theor Chim Acta (Berl) **46**: 1; b) Bickelhaupt FM, Baerends EJ (2000) In: Lipkowitz KB, Boyd DB (eds) Reviews in Computational Chemistry, vol 15. Wiley-VCH, New York, chapter 1 and references cited therein
[4] Pauling L (1931) J Am Chem Soc **53**: 1367
[5] Pauling L (1975) Proc Nat Acad Sci USA **72**: 4200
[6] Pauling L (1976) Proc Nat Acad Sci USA **73**: 274
[7] Frenking G, Fröhlich N (2000) Chem Rev **100**: 717
[8] Glerup J, Monsted O, Schäffer CE (1976) Inorg Chem **15**: 1399
[9] Smith DW (1978) Structure and Bonding **35**: 87
[10] a) te Velde G, Bickelhaupt FM, Baerends EJ, Fonesca Guerra C, van Gisbergen SJA, Snijders JG, Ziegler T (2001) J Comput Chem **22**: 931; b) ADF program, release ADF2004.01, web site: http://www.scm.com
[11] a) Bader RFW (1990) Atoms in Molecules. A quantum theory. Oxford University press, Oxford, and references cited therein; b) *Xaim-1.0* – a X11 graphical user interface to several programs based on some aspects of the theory of atoms in molecules (EXTREME and FLOPO, interfaced to ADF2004.01), José Cralos Ortiz Alba and Carles Bo Jané, Department de Quimica Fisica I Inorganica Universitat Rovira I Virgili, Taragona, Spain; http://www.quimica.urv.es/ADF_UTIL, free domain

[12] Becke AD, Edgecombe KE (1990) J Chem Phys **92**: 5397
[13] Silvi B, Savin A (1994) Nature **371**: 683
[14] Savin A, Jepsen O, Flad J, Anderson OK, Preuss H, von Schnering HG (1992) Angew Chem Int Ed Engl **31**: 187
[15] a) Kohout M (2004) Int J Quant Chem **97**: 651; b) Kohout M (2004) Programs *Basin* and *Dgrid* (interfaced to ADF), version 2.4. Max Planck Institute for Chemical Physics of Solids, Dresden, free available from kohout@cpfs.mpg.de
[16] a) Savin A, Silvi B, Colonna F (1996) Can J Chem **74**:1088; b) Noury S, Colonna F, Savin A, Silvi B (1998) J Mol Struct **450**: 59; c) Silvi B (2004) Phys Chem Chem Phys **6**: 256; d) Pilme J, Silvi B, Alikhani ME (2003) J Phys Chem A **107**: 4506
[17] Jørgensen CK (1962) Absorption spectra and chemical bonding in compexes. Pergamon Press, Oxford
[18] Cremer D, Kraka E (1984) Angew Chem Int Ed Engl **23**: 627
[19] Shaik S, Maitre P, Sini G, Hiberty PC (1992) J Am Chem Soc **114**: 7861
[20] Kutzelnigg W (1991) In: Maksic ZB (ed) Theoretical Models of Chemical Bonding, vol 2. Springer, Berlin, pp 1–44
[21] Fradera X, Austen MA, Bader RFW (1999) J Phys Chem A **103**: 304
[22] Silvi B, Pilme J, Fuster F, Alikhani ME (2003) In: Russo N et al. (eds) Metal Ligand Interactions. Kluwer, pp 241–284
[23] Calatayud M, Andrés J, Beltran A, Silvi B (2001) Theor Chem Acc **105**: 299
[24] Gillespie RJ, Noury S, Pilmé J, Silvi B (2004) Inorg Chem **43**: 3248
[25] Häussermann U, Wengert S, Nesper R (1994) Angew Chem Int Ed Engl **33**: 2073
[26] Santos JC, Tiznado W, Contreras R, Fuentealba P (2003) J Chem Phys **120**: 1670
[27] Silvi B, Kryachko ES, Tishchenko O, Fuster F, Nguyen MT (2002) Mol Phys **100**: 1659
[28] Jørgensen CK, Pappalardo R, Schmidtke H-H (1963) J Chem Phys **39**: 1422
[29] Schäffer CE (1968) Structure and Bonding **5**: 67
[30] Figgis BN (1987) In: Wilkinson G (ed) Comprehensive Coordination Chemistry, vol 1. Pergamon Press, Oxford, p 225
[31] Schönherr T, Atanasov M, Adamsky H (2003) In: Comprehensive Coordination Chemistry, vol 2, p 443
[32] Vanquickenborne LG, Ceulemans A (1981) Inorg Chem **20**: 796
[33] Smith DW (1977) Inorg Chim Acta **22**: 107
[34] Klamt A, Schürrmann G (1993) J Chem Soc Perkin Trans 2, 799
[35] Pye CC, Ziegler T (1999) Theor Chem Acc **101**: 396
[36] Atanasov MA, Reinen D (2004) Inorg Chem **43**:1998
[37] Penka Fowe E (in preparation) PhD Thesis, Univ Fribourg
[38] Tregenna-Piggott PLW, Best SP, Güdel HU, Weihe H, Wilson CC (1999) Solid State Chem **145**: 460
[39] Tregenna-Piggott PLW, Weihe H, Bendix J, Barra A-L, Güdel H-U (1999) Inorg Chem **38**: 5928
[40] Spichiger D, Carver G, Dobe C, Bendix J, Tregenna-Piggott PLW, Meier R, Zahn G (2001) Chem Phys Lett **337**: 391
[41] Wang SG, Schwarz WHE (1998) J Chem Phys **109**: 7252
[42] a) Cotton FA, Curtis NF, Johnson BFG, Robinson WR (1965) Inorg Chem **4**: 326; b) Cotton FA, Harris CB (1965) Inorg Chem **4**: 330; c) Cotton FA (1965) Inorg Chem **4**: 334
[43] Heitler W, London F (1927) Z für Physik **44**: 455
[44] Coulson CA, Fischer I (1949) Philosophical Magazine **40**: 386
[45] Cotton FA, Nocera DG (2000) Accounts of chemical research **33**: 483, and references cited therein
[46] Llusar R, Beltrán A, Andrés J, Fuster F, Silvi B (2001) J Phys Chem A **105**: 9460
[47] Bursten BE, Clayton TW Jr (1994) Journal of Cluster Science **5**: 157

[48] Anderson PW (1959) Phys Rev **115**: 2
[49] Hay PJ, Thibeault JC, Hoffmann R (1975) J Am Chem Soc **97**: 4884
[50] Atanasov M, Daul CA (2003) Chem Phys Lett **379**: 209
[51] Mayer I (1983) Int J Quantum Chem **XXIII**: 363
[52] Mayer I (2000) Chem Phys Lett **332**: 381
[53] Mayer I (2003) Chem Phys Lett **382**: 265
[54] Gerloch M, Constable EC (1994) Transition metal chemistry. The valence shell in d-block chemistry. VCH, Weinheim New York
[55] Weinhold F, Landis CR (2001) Chemistry education: research and practice in Europe **2**: 91
[56] Landis CR, Cleveland T, Firman TK (1995) J Am Chem Soc **117**: 1859
[57] Landis CR, Firman TK, Root DM, Cleveland T (1998) J Am Chem Soc **120**: 1842
[58] Weinhold F, Landis CR (book announced in Ref. 45)
[59] Weinhold F (2003) Angew Chem Int Ed Engl **42**: 4188
[60] Cybilsky SM, Scheiner S (1990) Chem Phys Lett **166**: 57
[61] Glendening ED, Steitwieser A (1994) J Chem Phys **100**: 2900